A sub-millimetre two-wavelength EDM that compensates the air refractive index: uncertainty and measurements up to 5 km

Joffray Guillory, Daniel Truong, Jean-Pierre Wallerand, Christophe Alexandre

Joffray Guillory, Daniel Truong, Jean-Pierre Wallerand, Christophe Alexandre. A sub-millimetre two-wavelength EDM that compensates the air refractive index: uncertainty and measurements up to 5 km. Measurement Science and Technology, 2023, 35 (2), pp.025024. 10.1088/1361-6501/ad0a22 . hal-04331758

Measurement Science and
Technology

100 year anniversary
Measurement Science and Technology

PAPER • **OPEN ACCESS**

A sub-millimetre two-wavelength EDM that compensates the air refractive index: uncertainty and measurements up to 5 km

To cite this article: Joffray Guillory *et al* 2024 *Meas. Sci. Technol.* **35** 025024

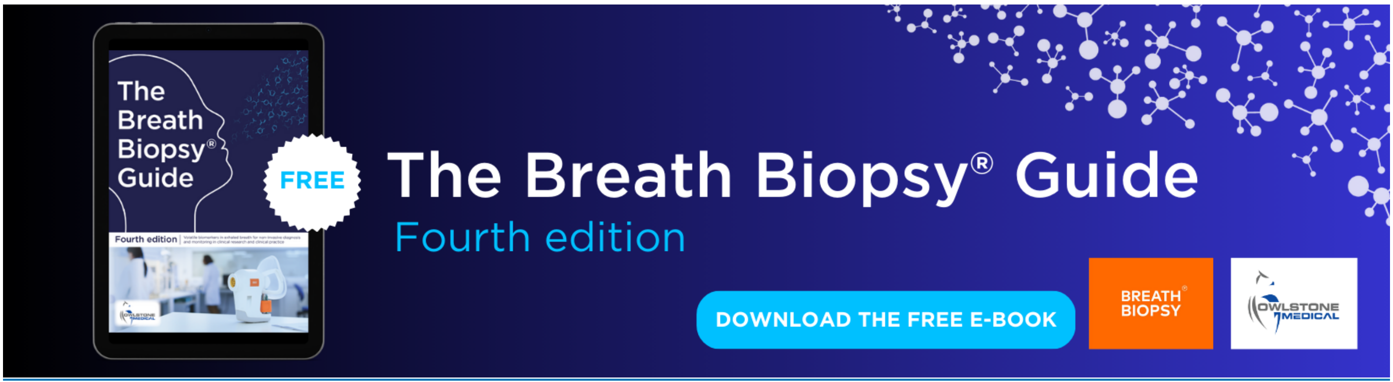

OPEN ACCESS
IOP Publishing
Measurement Science and Technology
Meas. Sci. Technol. 35 (2024) 025024 (21pp)
https://doi.org/10.1088/1361-6501/ad0a22

A sub-millimetre two-wavelength EDM that compensates the air refractive index: uncertainty and measurements up to 5 km

Joffray Guillory[1,*], **Daniel Truong**[1], **Jean-Pierre Wallerand**[1] **and Christophe Alexandre**[2]

[1] Conservatoire National des Arts et Métiers (Cnam), Laboratoire commun de métrologie LNE-Cnam, 1 rue Gaston Boissier, 75015 Paris, France
[2] Conservatoire National des Arts et Métiers (Cnam), Centre d'Etudes et De Recherche en Informatique et Communications (CEDRIC), 292 rue Saint-Martin, 75003 Paris, France

E-mail: joffray.guillory@cnam.fr

Received 14 April 2023, revised 23 October 2023
Accepted for publication 6 November 2023
Published 16 November 2023

Abstract

Distance measurements over several kilometres with a sub-millimetre uncertainty are required for deformation monitoring in fields such as geodesy or civil engineering where well-controlled scale is critical. This paper presents a two-wavelength electro-optical distance meter (EDM) capable of such measurements and traceable to the SI (Système International d'unités). It is based on simultaneous measurements of optical path lengths, at two wavelengths, one at 780 nm and the other at 1560 nm, the dispersion between the two wavelengths allowing real-time compensation of the air refractive index along the optical paths. The uncertainty budget of this EDM has been established, taking into account both the telemetric and the mechanical contributions. One of the main sources of errors is crosstalk, which originates mainly from the optical splitters acting as circulators and becomes more pronounced for lower received powers over longer distances. For signal-to-crosstalk ratios (SCRs) higher than 60 dB, the instrumental uncertainty in the air-index compensated distance was assessed to be 320 µm ($k = 1$). In the field, two distance measurements, one over 2.6 km, the other over 5.4 km, were carried out over a period of up to 6 days, and for a temperature and pressure varying by as much as 10 °C and 17 hPa. For each distance, the standard deviation of the Gaussian fit of the experimental points was less than 250 µm. This level of refractivity compensation demonstrates that the developed instrument works properly. In addition, standard deviations lower than 140 µm were achieved for displacement measurements at distances around 2.6 km and 5.4 km. All these results were obtained for SCRs higher than 60 dB. Finally, solutions are proposed for mitigating the effect of high crosstalk values on instrumental uncertainty.

Keywords: absolute distance meter, length metrology, two-wavelength telemetry, refractive index compensation, distance measurement

---

[*] Author to whom any correspondence should be addressed.

1. Introduction

Deformations of a few millimetres or less per year over distances of several hundred meters or several kilometres remain difficult to detect, especially over short time periods. Measuring them is however of great importance for the monitoring of civil engineering structures such as bridges [1], power plants [2] and tunnels [3], or the study of geological formations such as glaciers [4], volcanoes and faults [5], e.g. for the prediction of earthquakes [6]. Equally accurate measurements are also required for the construction and monitoring of large-scale facilities such as particle accelerators [7] or calibration baselines [8].

Nowadays, Global Navigation Satellite Systems (GNSS) are commonly used for such applications. GNSS-Based Distance Meters (GBDM) achieve an accuracy of the order of a few millimetres. However, their SI (Système International d'unités) traceability to the metre is difficult to establish [9–11]. In this case, the use of optical telemetry can help provide a well-defined traceable metrological scale for the GBDM or replace it on an occasional basis.

The major challenge for the optical telemetry lies in the determination of the air refractive index, which depends not only on the vacuum optical wavelength λ, but also on the air temperature T, the pressure p, the partial pressure of water p_ω, and the CO_2 content x. It is usually calculated using the semi-empirical Edlén equation [12], similar updated formulas such as that of Bönsch and Potulski [13], or the Ciddor equation recommended by the International Association of Geodesy [14–16]. More recently, new formulas have been proposed such as that of Voronin and Zheltikov [17]. With such an approach, and using conventional weather sensors, obtaining an accuracy better than 1 ppm for distances greater than 1 km is almost impossible owing to inhomogeneity of the aforementioned atmospheric parameters, especially temperature in the atmosphere. The air refractive index varies in time and space. The contributions of the average temperature, pressure and CO_2 content along an optical path to a measured optical distance are, respectively, -0.95 mm km^{-1} per °C, 0.27 mm km^{-1} per hPa, and 0.03 mm km^{-1} per 200 ppm.

To overcome this problem, a two-wavelength technique is sometimes used. This concept, originally proposed in the 1960s [18, 19], allows one to perform the first velocity correction. Its principle involves two simultaneous optical path length measurements D_1 and D_2 at respective wavelengths λ_1 and λ_2. It is assumed light at each wavelength travels along the same path and is in the same atmosphere. Thus, with the conventional approach, the geometrical length L travelled by the optical waves is:

$$L = \frac{D_1}{n(\lambda_1, T, p, x, p_\omega)} = \frac{D_2}{n(\lambda_2, T, p, x, p_\omega)} \quad . \tag{1}$$

By contrast with the two-wavelength technique, it is calculated using:

$$L = D_1 - \frac{n(\lambda_1, T, p, x, p_\omega) - 1}{n(\lambda_2, T, p, x, p_\omega) - n(\lambda_1, T, p, x, p_\omega)} \left(D_2 - D_1\right) \quad . \tag{2}$$

In such a case, L is referred to the dispersion-based air-index compensated distance. To illustrate the advantage of this approach, we take the semi-empirical Edlén equation, where the dependencies on wavelength and environmental parameters can be separated in a model of the form:

$$n\left(\lambda,\ T,\ p,\ x,\ p_\omega\right) - 1 = K\left(\lambda\right) \cdot D\left(T, p,\ x\right) - p_\omega g\left(\lambda\right) \tag{3}$$

where $K(\lambda)$ represents the wavelength-dependent dispersion term, $D(T, p, x)$ the density term, and $g(\lambda)$ the humidity term.

According to Meiners-Hagen and Abou-Zeid [20], the compensated distance in formula (2) can then be written as:

$$L = \frac{K(\lambda_1) D_2 - K(\lambda_2) D_1}{K(\lambda_1) - K(\lambda_2) + p_\omega \times \left(g(\lambda_1) \cdot K(\lambda_2) - g(\lambda_2) \cdot K(\lambda_1)\right)} \quad . \tag{4}$$

To derive formula (4), we assume the integrals of the density terms $D(T, p, x)$ along the two paths are the same.

It appears that the formula giving the compensated distance no longer depends on the temperature, pressure or CO_2 content, but only on the partial pressure of water p_ω. In dry air, formula (2) can be simplified to:

$$L = D_1 - A\left(\lambda_1, \lambda_2\right) \times \left(D_2 - D_1\right) \tag{5}$$

where the factor A depends only on the chosen wavelengths:

$$A\left(\lambda_1, \lambda_2\right) = \frac{n(\lambda_1, T, p, x, p_\omega) - 1}{n(\lambda_2, \ldots) - n(\lambda_1, \ldots)} = \frac{K(\lambda_1)}{K(\lambda_2) - K(\lambda_1)} \quad . \tag{6}$$

As can be seen in formula (5) which applies to dry air, the critical point in a two-wavelength distance meter is to be able to measure very accurately the optical path lengths, and especially the length difference between the two optical paths. For a given uncertainty on D_i, the final uncertainty in the air-index compensated distance L is degraded by the factor A. If we assume the factor A has no uncertainty, i.e. one considers only the instrumental errors, the uncertainty in the compensated distance L is:

$$\begin{aligned} u(L)^2 &= u(D_1)^2 + A^2 \times u(D_2 - D_1)^2 \\ &\quad - 2\,A \times \mathrm{cov}\left(D_1; D_2 - D_1\right) \\ &= \left(1 + 2\,A\right) \times u(D_1)^2 + A^2 \times u(D_2 - D_1)^2 \\ &\quad - 2\,A \times \mathrm{cov}\left(D_1; D_2\right) \\ &\simeq A^2 \times u(D_2 - D_1)^2 \text{ for } A \gg 1. \end{aligned} \tag{7}$$

It should be noted that even for wet air, the multiplying effect of the factor A on the uncertainty remains a good approximation. To minimise this factor, it is desirable to work if possible with shorter wavelengths, where the dispersion is greatest, for example in the visible rather than in the infrared. It is also important that the two wavelengths be as distant as possible. Finally, the two-wavelength approach is valid for both phase index, that appears in interferometric measurements, and group index, that governs measurements performed by electro-optical distance meters (EDMs).

The first developments of EDMs exploiting this technique took place in the early-to-mid 1970s and used red light at

632.8 nm from He-Ne lasers and either blue light at 441.6 nm from He–Cd lasers or near ultra-violet light at 361.8 nm provided by mercury arc lamps [21, 22]. The laser beams were sinusoidally modulated at a frequency of several gigahertz by an optical crystal modulator, and then demodulated by a second pass through the same modulator after their round trip to the distant retroreflector. The modulation frequency was adjusted to receive a minimum of light from the photodetectors, which means that the phase differences between transmitted and received signals were 180° out of phase, as in the Fizeau experiment. With such a technique, what matters is the group refractive index of the air. This two-wavelength approach was then applied in the 1980s with the commercial Terrameter EDM [7, 23]. This instrument, using wavelengths at 441.6 nm and 632.8 nm for a factor A of 21, was able to measure a distance of 10 km to within ±1 mm. In the same period, a two-colour Geodimeter was also developed, the performance of which was similar with an uncertainty of roughly 1.2 mm for a 10 km baseline [6]. These EDMs, produced in very limited series, are no longer in operation owing their complicated design and operating procedure that made them somewhat difficult to use.

More recently, several types of instruments have implemented this technique. For example, we can mention the development of a homodyne interferometer [20], or the TeleYAG and TeleYAG II multi-wavelength heterodyne interferometers which allow the measurement of absolute distances [24, 25]. The latter use frequency-doubled Nd:YAG lasers that provide wavelengths at 1064 nm and 532 nm for a factor A of about 65 (phase index). We can also mention the use of optical frequency combs, which generate simultaneously light at very many wavelengths. With such a tool, optical path lengths can be determined by measuring the electronic phase of intermode beats of the frequency combs [26, 27], or by performing pulse-to-pulse interferometry [28]. These systems use wavelengths in bands at 780 nm and 1560 nm for a factor A of about 48 or 142 depending on whether the group velocity [26] or the phase velocity [28] is considered, but also wavelengths at 590 nm and 890 nm with a factor A of 35 for group velocity [27]. While all these instruments have provided good results, none have demonstrated their performances for measurements over distances of several kilometres.

This paper presents a modern version of a two-wavelength instrument. It is based on radio-frequency (RF) phase measurements of amplitude-modulated lights, which is a suitable approach for distances of several kilometres as proven by the renowned Terrameter. Our instrument uses wavelengths at 780 nm and 1560 nm. The low dispersion between these wavelengths leads to a rather large factor A of 48. Thus, at each wavelength, an uncertainty measurement better than 20 µm in the optical path lengths is required to reach an uncertainty of 1 mm in the air-index compensated distance. Dealing with such a large factor A is certainly challenging. Nevertheless, the wavelengths of our prototype are attractive due to the wide availability of affordable fibre-optic components in this range, especially at 1560 nm, which is standard in the telecommunication industry.

The rest of this paper is organised as follows. In section 2, the two-wavelength EDM is presented. In section 3, the instrumental uncertainty for the measurement of dispersion-based air-index compensated distances is estimated. In section 4, the instrument and its uncertainty are validated through characterisations over short distances, up to 100 m, indoors, then outdoors over 2.6 km and 5.4 km. Displacements were measured for all three ranges. For the two long distances, measurements were performed over several days to verify the long-term stability of the instrument and thus its ability to compensate for changes in the air refractive index.

2. Presentation of the two-wavelength EDM

2.1. Principle

The instrument developed involves a well-known technique: a light beam intensity modulated by a RF wave, is sent in air to a distant target, retroreflected, and finally detected by a photodetector located close to the source. The distance to be measured is thus proportional to the phase delay measured between the RF waves detected after propagation in air and the emitted one,

$$L = \frac{1}{2} \times \left(\frac{\phi}{2\pi} + k\right) \times \frac{c}{n \times f_{\mathrm{RF}}} \tag{8}$$

where ϕ the measured RF phase delay wrapped into the interval $[-\pi, +\pi]$, k an integer number corresponding to the number of times that this phase has rotated by 2π during its propagation, c the speed of light in vacuum, n the group refractive index of air, and f_{RF} the modulation frequency of the light. In practice, the number k of synthetic wavelengths $c/(n \times f_{\mathrm{RF}})$ is deduced from several distance measurements performed at different RF values. The factor 1/2 in formula (8) is the result of the round trip of the light.

2.2. Design of the prototype

The two-wavelength approach was implemented at 779.8 nm and 1559.6 nm. The developed prototype is presented in figure 1. It is compact, easily transportable, and thus ready for field measurements.

The setup of the two-wavelength telemeter is depicted in figure 2. A laser diode emits an optical carrier near 1560 nm, which is intensity-modulated by a RF at 5060.75 MHz using an electro-absorption modulator (EAM), then amplified with an optical amplifier. From this first signal, a second one at 780 nm is obtained by frequency doubling in a non-linear periodically poled lithium niobate (PPLN) waveguide. This second-harmonic generation results in a signal at half the wavelength of the pump at 1560 nm, with the same modulation frequency. Each of these optical signals passes through an optical splitter acting as a high-isolation circulator, before being transported to the optical head by means of a single-mode optical fibre. At this point, the optical powers are about 180 mW and 20 mW for the wavelengths at 780 nm and 1560 nm, respectively.

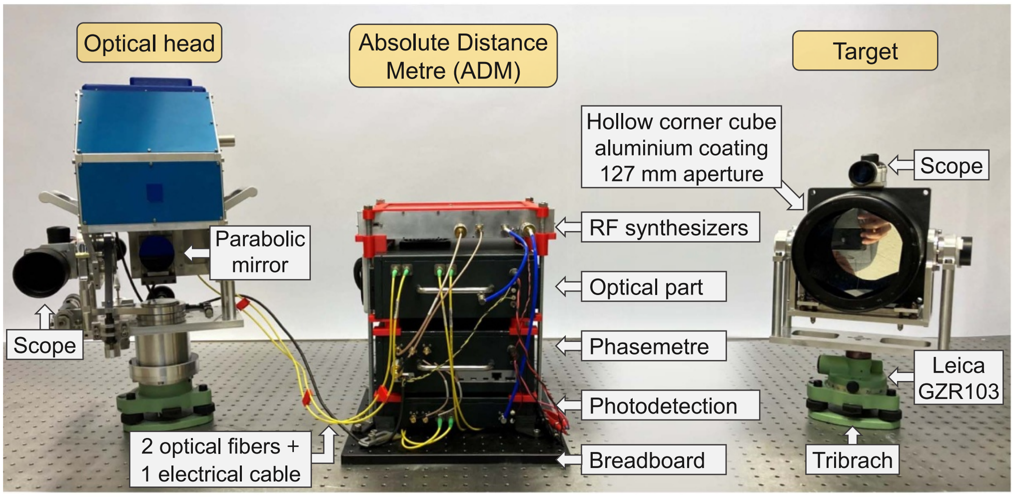

Figure 1. Overview of the two-wavelength electro-optical distance meter.

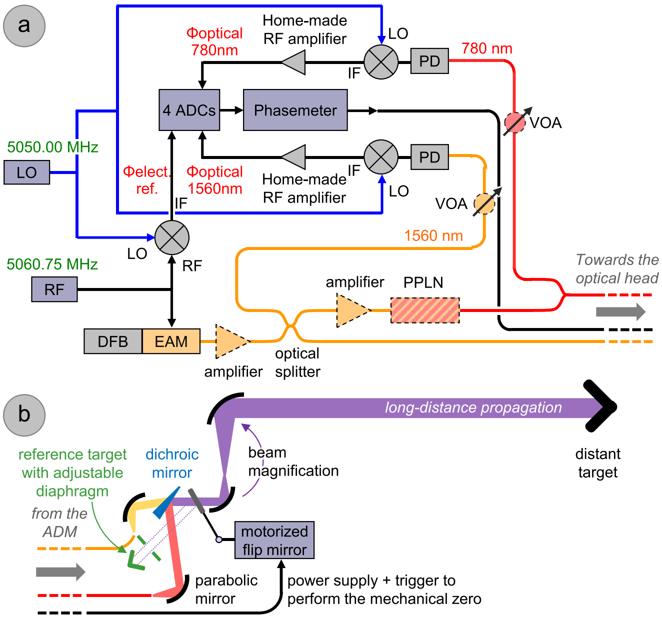

Figure 2. Schematic of the two-wavelength EDM: (a) fibre-optic absolute distance meter; (b) optical head for combination and collimation of the two optical beams at 780 nm and 1560 nm.

The two optical beams are combined inside the optical head: in figure 2(b) after emission in free space and collimation by off-axis parabolic mirrors, the beam at 1560 nm passes through a dichroic mirror (with mirror faces not parallel, i.e. a wedge mirror, to avoid multiple reflections between two surfaces), while that at 780 nm is reflected by it. Once the beams are superimposed, a pair of parabolic mirrors magnifies the diameters of the two spots by a factor of 10.2 to obtain, respectively, values of 28.0 mm and 29.0 mm (diameters being defined as twice the distance from the spot centres to where the intensity drops to $1/e^2$ of the maximum value) at 780 nm and 1560 nm. The sizes of the spots increase with the distance, due to the divergence of the Gaussian beams. At distances of 1.37 km at 780 nm and 0.70 km at 1560 nm, they are twice as large. At 5 km, the spot sizes have increased relative to emitted signals by a factor 6.4 and 11.8 at, respectively, 780 nm and 1560 nm. Finally, both the divergence of the Gaussian beams and the attenuation through the air reduce the optical power densities (expressed in W m^{-2}) received on the target side, and therefore the laser risk to eyes.

After propagation up to the hollow corner cube, the two beams come back to the telemeter to be reinjected into the same fibres as previously. After a second pass through their respective optical splitter, the two laser beams are directed towards their photodiode (PD). At this point, a local oscillator (LO) converts the RF signals at 5 GHz into an intermediate frequency (IF) of 10.75 MHz. They are finally amplified by 70 dB and converted by analogue to digital converters (ADCs) operating at 250 MSa s^{-1} with a resolution of 14 bits. The distances are then calculated from the phase difference between these measurement signals and an electrical reference built from the direct mixing of the RF and LO carriers. The signals are processed digitally by a field-programmable gate array (FPGA) designed by our group and displayed using Matlab$^{\mathrm{TM}}$ software.

As shown in figure 2(b), a motorized flip mirror has been implemented to deviate the free-space optical beams towards a small reference corner cube and thus compensate for the phase variations induced by temperature changes in the opto-electronic, fibre-optic and microwave components. In practice, this mechanical zero measurement is performed every second when the RF power received by the system is sufficient to perform a distance measurement.

Fibre-guided variable optical attenuators (VOAs) are used to adapt the RF power of the received signals, ideally around −5 dBm. The attenuation levels are therefore high for short distances, and low for long distances. These VOAs, placed just before the photodetectors, introduce additional delays, which depend on their level of attenuation. To avoid biases on the distance measurements, the attenuation levels must be constant

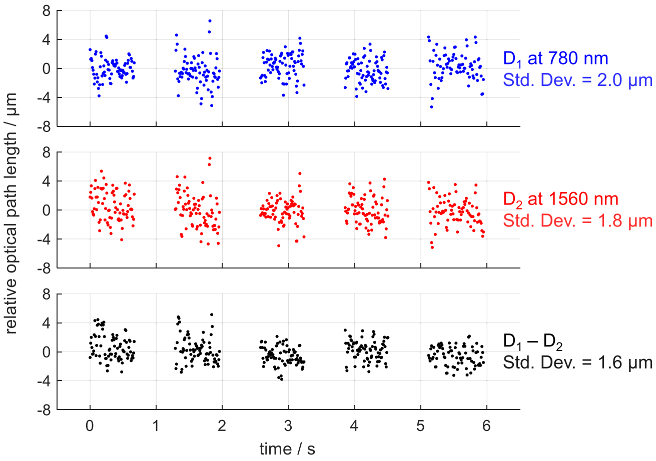

Figure 3. Optical path length measurements at 780 nm and 1560 nm over 1 m, and their difference.

between the measurement of the distant target and that of the reference target. For this purpose, an adjustable optical diaphragm was placed in front of the reference target. Note that if the attenuation levels differ between the two paths, changes in the measured distances are observed over the long term: it is this phenomenon that was noticed in the first measurements made by our two-wavelength EDM and presented in [29].

Finally, the optical head used for combination and collimation of the two optical beams is a gimbal mechanism able to aim at the distant target. Similarly, the distant target is a corner cube mounted on a gimbal mechanism. The weight of the absolute distance meter (ADM) is 22.8 kg, which includes a breadboard of 6.0 kg, and the weight of the head is 9.3 kg. The instrument, powered by 230 V a.c. supply, consumes less than 160 W (maximum value observed, at start-up), with a typical value in operation around 135 W.

2.3. *Measurement of the optical path lengths*

As an example, figure 3 shows the measurement of a short distance of 1 m in a controlled environment ($T = 22.3$ °C, $P = 1004.95$ hPa, $RH = 49.3\%$). It represents the optical path lengths at 780 nm and 1560 nm used in formula (2), shown as relative values for easier reading of the curves: only length variations are depicted, not absolute lengths even though the values of the latter are known, in order to estimate the system resolution.

For each measurement, five packets of 75 points were recorded, with 20 ms of integration time per point. Between these packets, a length measurement of the reference target was performed to compensate for possible distance variations. In the end, the standard deviations of these curves are equal to 2.0 µm and 1.8 µm for measurements at, respectively, 780 nm and 1560 nm. These values correspond to the random noise of the ADM. The two optical path length measurements are partially correlated since the standard deviation of their difference is only 1.6 µm rather than 2.7 µm (the square root of the sum of the variances).

It should be noted that an integration time of 20 ms corresponds to the order of magnitude of the time scale of the atmospheric turbulences, i.e. the amount of time during which signal levels remain essentially constant [30].

3. Uncertainty of the two-wavelength EDM

To determine the uncertainty of the dispersion-based air-index compensated distance, one must first know the uncertainty of the optical path lengths for each wavelength separately as shown in formula (2). We divided this into two main components: the telemetric part and the mechanical part. It has to be emphasized that we only consider uncertainty components coming from the instrument itself, and not those coming from the determination of the air refractive index for distance measurements performed at a single wavelength or those from the dispersion-based model in formula (4) for distance measurements performed at two-wavelength.

3.1. *The telemetric part*

In this section, the uncertainty related to the ADM is established on the basis of our previous study [31]. Thus, for a distance measured with a single wavelength, four uncertainty components were quantified: modulation frequency, crosstalk, amplitude-to-phase coupling at photodetection, and phase measurement noise.

As shown in formula (8), the traceability of the measurement to the SI metre is ensured by the knowledge of the modulation frequency. This is generated by a synthesizer locked to a rubidium (Rb) clock (Microsemi model SA.22c). The relative aging rate of the clock frequency is ±4.8 10^{-10} per year. By measuring annually, then correcting the frequency delivered by the synthesizer, one can guarantee a relative error in the modulation frequency of less than 5 10^{-10}. Lastly, the second synthesizer used for the frequency down-conversion, as well as the phasemeter, are also locked to the same Microsemi Rb clock signal.

Crosstalk is the effect to which the two-wavelength technique is the most sensitive. It arises from an unwanted transfer of the measurement signal to the phasemeter, for instance due to a poor electromagnetic shielding between the emission and detection stages, or from the limited isolations of the optical beam splitters that act as circulators. Crosstalk induces a cyclic error on the distance measurements that depends on two parameters, namely the phase and the amplitude of the crosstalk signal with respect to the measurement signal. Thus, the period of the cyclic error is equal to half the synthetic wavelength, i.e. about 29.6 mm, and its amplitude $A_{\text{crosstalk}}$ (half peak-to-peak) is a function of the signal-to-crosstalk ratio (SCR) expressed in decibels:

$$A_{\text{crosstalk}} = \frac{1}{4\pi} \times \frac{c}{f_{\text{RF}}} \times 10^{-\text{SCR}/20} \quad . \tag{9}$$

An SCR higher than 60 dB corresponds to an uncertainty component below 3.3 µm (coverage factor k equal to 1).

Table 1. Uncertainty budget for optical path length measurements with the prototype of two-wavelength ADM.

Uncertainty component	Source of uncertainty	Value	Distribution	Uncertainty contribution
$u_{f_{\mathrm{RF}}}$	Values of the RF modulation	5060.75 MHz	Uniform	4.8×10^{-10} $L/(2 \times \sqrt{3})$ µm with L expressed in µm
$u_{\mathrm{crosstalk}}$	Presence of crosstalk	SCR from 50 dB to 60 dB	Arcsine	From $14.9/\sqrt{2}$ µm to $4.7/\sqrt{2}$ µm
$u_{\mathrm{AM/PM}}$	Variations of the signal amplitude	Amplitude variations up to 15 dB	Uniform	$0.15 \times 15/(2 \times \sqrt{3})$ µm
u_{random}	Random noise on the phase measurement	Std. Dev. ~ 0.4 mrad	Normal	2.0 µm at 780 nm and 1.8 µm at 1560 nm

However, a low SCR such as 50 dB can be observed in practice for long distance measurements, i.e. when the received RF power is low. In such a case, an uncertainty component of 10.5 µm ($k = 1$) is obtained. When the two-wavelength ADM is used in the field to measure distances of several kilometres, we optimize received RF powers by minimizing attenuations upstream of the PDs (see VOAs in figure 2). The crosstalk level is then relatively constant, around −65 dBm, and there is a direct link between received RF power and SCR: for example, when visibility is good, power levels can easily exceed −5 dBm, so SCRs will be more than 60 dB. The SCR is the parameter of interest, but it is not measured directly. In fact, for each wavelength, the RF power of the measurement signal is supplied by the phasemeter together with the phase shift ϕ in formula (1), while we determine the crosstalk level by masking the measurement signal and then measuring the residual signal level.

The phase measurement is affected the amplitude-to-phase coupling inside the high-speed PDs, where intensity variations of the modulated optical signals are converted into phase variations in the generated RF signals. To reduce this effect, we opted for positive-intrinsic-negative PDs, which are a type of detectors with a low sensitivity to this phenomenon as demonstrated in [32]. Typically, the variations of the RF signals observed by the phasemeter due to changes in the optical powers, for example caused by atmospheric perturbations, induce variations in the measured distances with a slope of −0.15 µm dB^{-1}. For long-distance measurements, these variations are of the order of 15 dB with a RF signal level between 0 dBm and −15 dBm.

Lastly, the random noise of the phasemeter limits the resolution of the ADM. Figure 3 quantifies this noise: over a short distance, in a controlled environment, without amplitude variation (no amplitude-to-phase coupling) and without distance variation (no visible crosstalk effect), standard deviations lower than 2 µm are obtained over 6 s and for 20 ms integration time per point. According to formula (8), this value corresponds to a phase noise of $2\pi/14\,800$ for a 5 GHz modulation frequency.

The uncertainty budget of the ADM is summarized in table 1. The dominant contribution is crosstalk.

The uncertainty related to the ADM was determined for each wavelength by propagating the different sources of errors listed above to the optical path lengths (formula (8) for $n = 1$). This was done using Monte-Carlo simulations with 10^6 datasets randomly generated according to the probability distributions defined in table 1 and for a distance of 5 km to fix the uncertainty contribution of the RF frequency. The resulting error distributions are shown in figure 4 for SCRs of 60 dB and 50 dB.

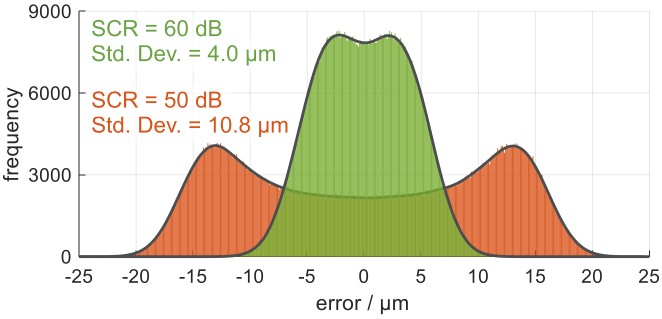

Figure 4. Distributions of the errors coming from the telemetric system for an optical path length measurement of 5 km performed at 780 nm. These results were obtained from Monte-Carlo simulations with SCRs of 50 dB and 60 dB. Similar results were obtained at 1560 nm.

If the system is well optimized and an SCR higher than 60 dB is reached, a measurement uncertainty of 4.0 µm ($k = 1$) over 5 km is achievable. However, for low SCR value such as 50 dB, as can sometimes be observed when received signal levels are low or when there is poor isolation in some components, a measurement uncertainty of 11 µm ($k = 1$) over 5 km is obtained.

In both cases, the double-peaked shape of the probability density functions come from the arcsine distribution of the crosstalk component. It was obtained by generating a crosstalk signal of fixed amplitude and random phase uniformly distributed over 2π. This is equivalent to assuming the phase of the crosstalk signal with respect to the measurement signal changes over time. However, if the phase shift was fixed, the error distributions would be a Gaussian with a non-zero mean value due to crosstalk and with a standard deviation dominated by the random noise on the phase measurement.

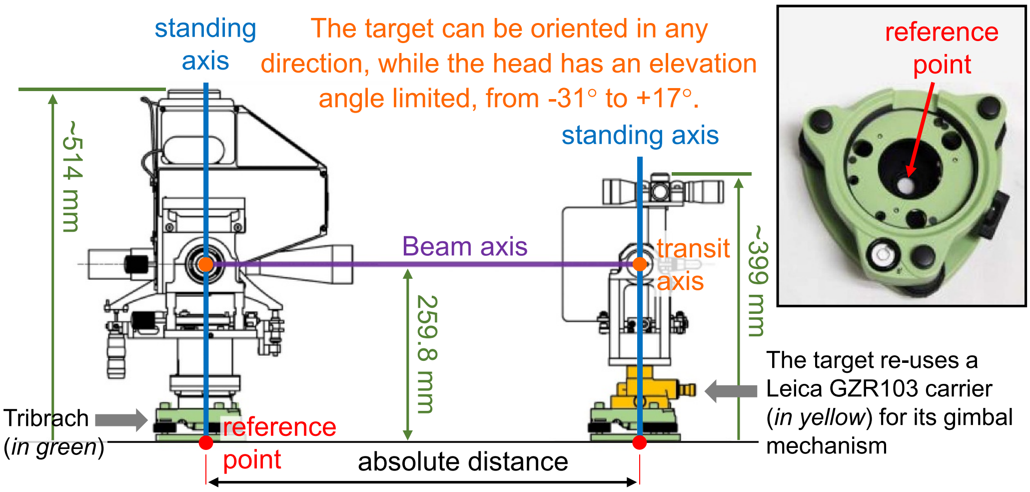

Figure 5. Measurement of absolute distances with the centres of the tribrach screws as geodetic markers.

3.2. The mechanical parts

In geodesy, distances are measured between two physical points called surveying markers, which can be for instance control points on the ground. In our case, we consider the simplest case where these physical points are the centres of the threads of the head and target tribrachs. This is depicted in figure 5.

As a consequence, to determine the uncertainty of an absolute distance, the mechanical sources of errors must be quantified. The majority of these errors listed below involve both the optical head and the target, and must therefore be counted twice.

3.2.1. Position repeatability. The repeatability of the positioning of the head and target when their carrier is clamped into a tribrach was tested. When the head was removed and clamped several times with unchanged levelling and orientation, the distance measurements performed between each positioning showed a standard deviation of 3.0 µm. In this experiment, in order to make measurements insensitive to the random noise of the phasemeter (last line in table 1), which is of the same order of magnitude, each distance measurement was averaged over 20 s. Then, the same operation for the target showed a standard deviation of 1.7 µm. These results agree with typical values of the literature [33]. However, they are only valid for a given pair of tribrach and carrier, and can vary slightly for other tribrachs. Thus, as a precaution, we ascribe a wider uncertainty of 5 µm ($k = 1$) for the positioning of the head and the target.

3.2.2. Levelling. The positioning is repeatable if both the head and the target are levelled, which we do by adjusting the three levelling thumbscrews of their tribrach, based on the observation of longitudinal spirit levels. In our case, the optical head is equipped with two spirit levels mounted orthogonally, while the gimbal mechanism of the target is based on a Leica GZR103 carrier with a built-in bubble level. A one-graduation error of these spirit levels corresponds to a levelling error of 0.4 mm at 1.0 m for the optical head and 0.5 mm at 1.5 m for the target. In practice, i.e. in the field, it is quite common to have errors up to 1 graduation if the measurement takes too long: this generally happens when there is sunlight, even when the instruments are protected by parasols, probably due to thermal expansion of the mechanical parts. It is thus advisable to level regularly. Thus, for laser beams at a height of 259.8 mm and an error of one graduation in the axis of the distance measurement, the measured distance is subject to an additive error of 104 µm for the head and 87 µm for the target. These errors were therefore taken into account using uniform distributions.

3.2.3. Centring errors. The positioning can be repeatable, but it is not necessarily reproduceable for different orientations of the head and the target if their standing axis is not aligned with the screw centre of the tribrach on which they are clamped. We have noticed that these centring errors depend on the tribrachs used, and can be as large as 320 µm. However, they can be characterized and so corrected for.

For instance, to determine the centring error of the head when it is clamped on a given tribrach, the distance up to a fixed target is measured with different azimuthal angles of the head. In practice, the tribrach of the head is rotated around its centre, and so the orientation of the head relative to its tribrach changes, by using an aluminium cylinder of the same diameter as that of the tribrach screw hole. This tool, and the distance measurements, are shown in figure 6.

The centring errors are cyclic errors. Amplitudes lower than 320 µm were observed experimentally for a set of eight characterisations of head-tribrach or target-tribrach pairs. Each time, the experimental points fitted their regression sine curve well with residuals of standard deviations around 9 µm for the head

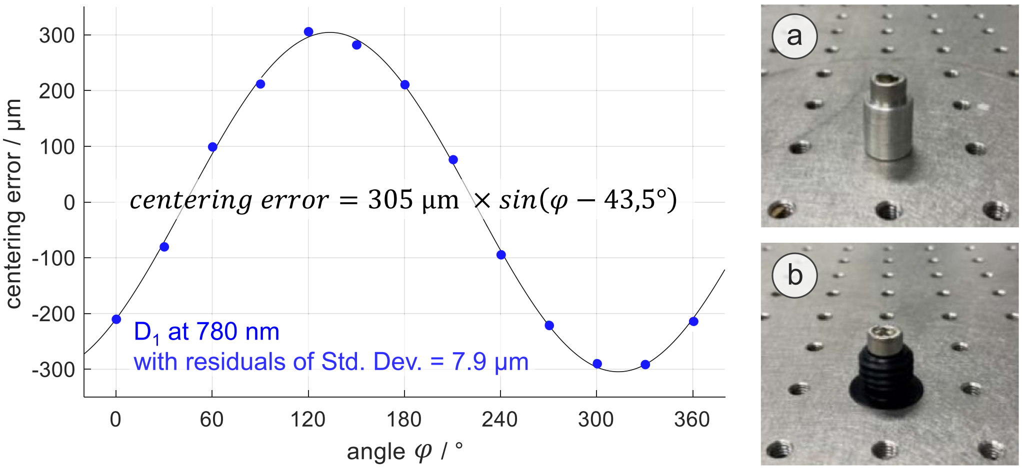

Figure 6. Example of a centring error measured with the optical head, which was rotated around its standing axis for 13 different orientations using the aluminium cylinder depicted in (a) instead of an ordinary screw used to fix the tribrach in (b). The azimuthal angle φ is indicated by the protractor mounted on the head.

and 15 µm for the target. The standard deviation is larger for the target owing to greater mechanical backlash on its standing axis based on a Leica GZR103 carrier.

In practice, distance corrections are applied as a function of the azimuthal angles, and uncertainties of normal distributions with standard deviations equal to those of the residuals are assumed.

3.2.4. Height difference. The optical head and the target were designed to have optical beams at the same height, 259.8 mm, plus or minus a few hundred micrometres (figure 5). The impact on the measured distances is thus negligible.

3.2.5. Instrument offset. The instrument offset is a constant added to the distance measurements to account for delays in cables, opto-electronic components, and optical paths. Such a correction is necessary in order for one to have an electro-optical origin that corresponds to the mechanical zero of the instrument, and thus be able to perform absolute distance measurements,

$$D_{\text{corrected}} = D_{\text{measured}} + O \tag{10}$$

where O is the instrument offset.

This offset can be determined by measurements on a small baseline composed of at least three aligned pillars [34]. With three pillars labelled P_1, P_2 and P_3, it is calculated as follows:

$$\begin{aligned} O &= D_{\text{measured}}\left(\|P_1 - P_2\|\right) \\ &\quad + D_{\text{measured}}\left(\|P_2 - P_3\|\right) - D_{\text{measured}}\left(\|P_3 - P_1\|\right) \\ &= D_{\text{corrected}}\left(\|P_1 - P_2\|\right) + O + D_{\text{corrected}}\left(\|P_2 - P_3\|\right) \\ &\quad + O - D_{\text{corrected}}\left(\|P_3 - P_1\|\right) - O. \end{aligned} \tag{11}$$

This is based on the fact that:

$$\begin{aligned} D_{\text{corrected}}\left(\|P_3 - P_1\|\right) &= D_{\text{corrected}}\left(\|P_1 - P_2\|\right) \\ &\quad + D_{\text{corrected}}\left(\|P_2 - P_3\|\right) \end{aligned} \tag{12}$$

which is true if the head and the target have beams at the same heights, if they are correctly levelled, and if we correct their centring errors. We recall that the target is a hollow corner cube mounted on gimbal mechanism, as shown in figure 1. The latter has the same height as the instrument, and its levelling and centring errors were characterized in the same way as the head.

In our case, four tribraches labelled A to D were mounted on an optical table in the alphabetical order, with ‖A–B‖ = 0.5 m, ‖A–C‖ = 1.3 m, and ‖A–D‖ = 2.4 m. All the distances were measured, from both sides. Thus, for each wavelength, 12 different distances and 8 different triplets were used to determine the instrument offset: its average value equals to −132.3221 mm at 780 nm and is 4.5 µm lower at 1560 nm as shown in figure 7. The corresponding standard deviations are around 25 µm, but they could be lower. Indeed, two points seem erroneous due to an error measurement in the distance from tribrach A to tribrach B.

This offset of about 13 cm is mechanical and is mainly due to the difference in distance between the measurement and reference paths. The offset portion of the measurement path goes from the motorized flip mirror in figure 2 to the invariant point of rotation of the optical head, while that of the reference path goes from the flip mirror to the reference target. Their theoretical values according to the mechanical design of the head are, respectively, 191 mm and 55 mm, plus or minus a few millimetres related to the adjustment of the reference target position. Thus, the offset should have been −136 mm, a value close to that obtained in figure 7. The difference of 4 mm with respect to the measurement is given as an indication only, and this value could be very different if a head were to be remade.

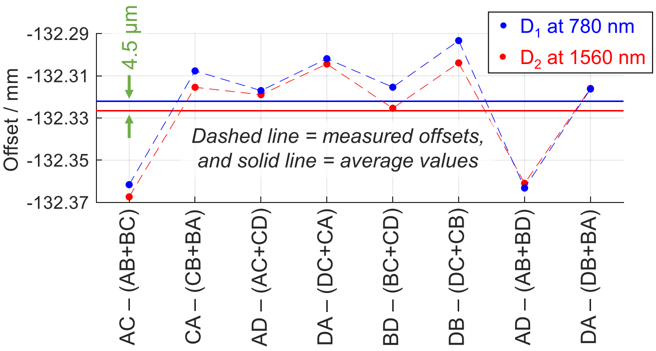

Figure 7. Results of the eight instrument offsets measured with a set of four tribrachs for the 780 nm wavelength.

What counts here is our ability to measure the instrument offset, and to ascribe an uncertainty to it.

3.2.6. *Invariant point of the optical head.*

The gimbal components designed for the optical head and target are not perfectly aligned. The different types of errors that can be encountered, and that have an impact on the measured distances, were described in [35]. These are the beam offset, the beam tilt, and the transit offset. The beam offset arises when a laser beam does not emerge from the invariant point of rotation of the gimbal mechanism. The beam tilt occurs if a laser beam is emitted at an angle from the normal to the plane defined by the two rotation axes. Finally, the transit offset produced when axes of rotation do not intersect.

To determine these errors, 1.5 inch spherically mounted retroreflectors (SMRs) were set up on the rotatable optical head, then measured by a laser tracker (Leica AT401) for various orientations of the head. Basically, the trajectories of these retroreflectors allow one to model the geometry of the two rotation axes in three-dimensional space.

For instance, a target measured for a fixed elevation of the head and for more than 3 azimuths describes a circle whose centre is located on the standing axis of the head. In our case, three different azimuthal circles, all parallel, were determined as shown in figure 8. In the same way, a target measured at a fixed azimuth and for more than three elevations describes a circle whose centre is located on the transit axis of the head. This time, four different elevation circles were determined. For the azimuthal angles, the measurement range was up to 290°, while for the angles of elevation, it was up to 48°.

In practice, each axis, defined by a vector n_a and a point p_a, was determined by a least-squares method: this consists in searching for circles C_k located in planes of normal n_a, and centred on points c_k located along a given line of direction n_a, such that the sum of the squares of the distances between the positions of the measured targets and the circles is minimised. The residuals of the least-squares minimizations have shown errors less than 62 µm, except for two points with errors of 113 µm and 166 µm, with a standard deviation of the residuals of 23 µm. The centring error of the SMR, as specified by the manufacturer, is 0.05 mm, which might explain the observed errors. The laser tracker employed also contributes to the observed errors, with maximum permissible errors of ± 10 µm for the measured distances and ± 15 µm + 6 µm m^{-1} for measured angles (after conversion into distances).

Finally, the orthogonality of the two rotation axes of the optical head is almost perfect with an angle of 89.92° (versus 90°). The transit offset is small with a distance between the two rotation axes of only 73 µm. This causes an offset in the distance measurements already included in the instrument offset.

As shown in figure 8, the optical axis of the overlapping beams at 780 nm and 1560 nm was also measured. For this purpose, it was materialized by a corner cube mounted on a displacement rail. In reality, the head was placed in the alignment of the rail prior to the measurements with the laser tracker. To achieve this, its position was optimised so that, whatever the position of the corner cube for distances from the head up to 12 m, the RF power received after reflection from the target is always at its maximum value. Over such short distances, with spot sizes around 3 cm, a deviation of the beams from the centre of the target of 1.5 mm reduces the received RF powers by a factor of two. In practice, the alignment is therefore carried out to better than one millimetre. In the end, the laser tracker measured seven different positions of the corner cube corresponding to distances from the head between 3 m and 12 m, which allowed the optical axis to be located, and thus the beam offset to be determined.

The beam offset is significant with optical beams passing 1.07 mm above the transit axis and shifted by 2.27 mm from the standing axis. This induces a cosine error the impact of which is small. In addition, the optical beams of the ADM emerge almost orthogonally to the rotation axes of the head, with angles of 89.96° and 90.76° as shown in figure 8. It should be noted that the value of 90.76° is very uncertain since the optical axis and the transit axis were not measured consecutively: between these two measurements, the azimuthal angle differs, and even if we returned to the same angular position thanks to the protractor placed on the head, an error of up to 1° could occur. The procedure used to determine the rotation axes and the optical axis of the optical head must be improved in the future.

From the parameters defined in figure 8, and on the basis of the model developed in [35], the uncertainty contribution of the mechanical misalignments of the optical head on the measured distances was estimated to be 2 µm. This value was obtained by a Monte-Carlo simulation, which showed a normal error distribution.

It should be pointed out that the errors in the rotation axes, i.e. the transit offset and the orthogonality between them, would be of the same order of magnitude if such an instrument had to be rebuilt. This is based not only on the design of the head, but also on the way in which the head is mounted. In fact, a cross-shaped tool was made that materialises the axes of rotation so as to allow the correct alignment of their ball bearings. The values of beam offsets are given as an indication and would undoubtedly be very different if such a head dismantled and reassembled.

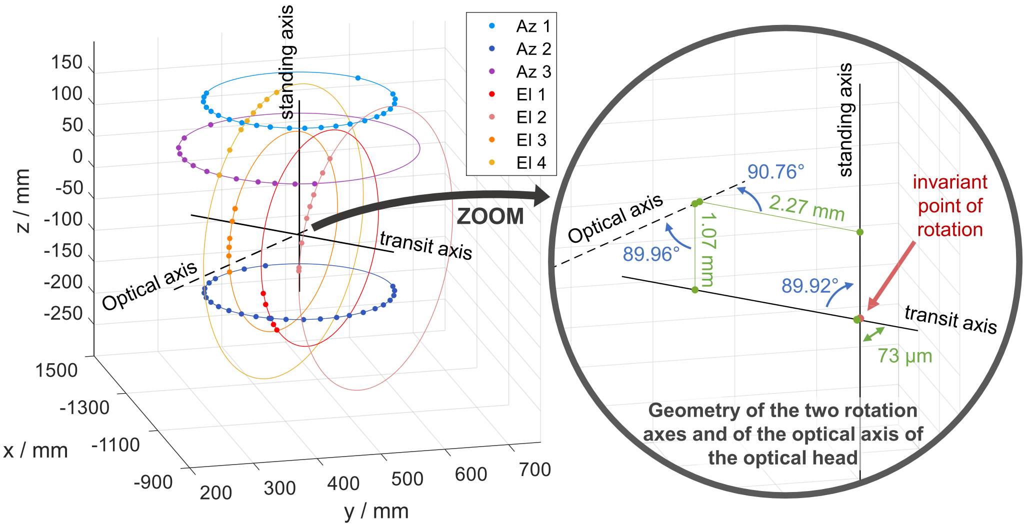

Figure 8. Trajectories of the targets mounted on the optical head in the laser tracker frame. This highlights the different types of misalignment errors: the beam offset, the beam tilt, and the transit offset.

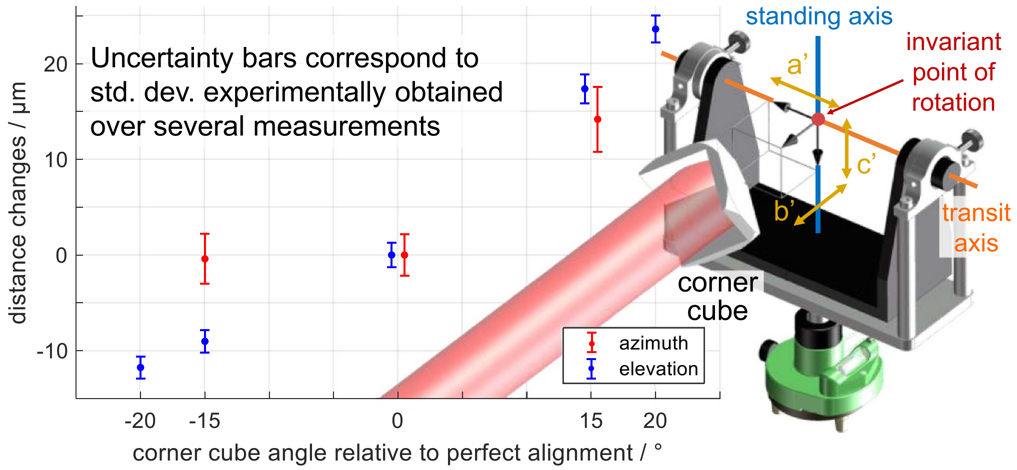
Uncertainty bars correspond to std. dev. experimentally obtained over several measurements

Figure 9. Variations of the measured distances as a function of the alignment of the corner cube with the optical head. This is used to determine the displacement of the corner cube relative to the invariant point of the target. The measured distances were about 1.5 m.

3.2.7. Invariant point of the target. Just as for the optical head, the mechanical errors of the target gimbal were estimated. First, the transit offset between the two rotation axes was determined using the double centring method [35], an approach possible with the target because it can be oriented in any direction. This consists in calculating the half difference between two successive distance measurements: a first one with the azimuthal and elevation angles such that $\theta = \varphi = 0$, then after rotations of 180° around the standing and transit axes, a second one with the orientation $\theta = \varphi = \pi$. A series of eight measurements yielded an average value of -4.9 µm with a standard deviation of 7.4 µm. In practice, we always use the corner cube with the same orientation, with the transit axis in front of the standing axis. This value is thus already included in the instrument offset.

In addition, the optical centre of the corner cube is not located at the invariant point of rotation of the gimbal mechanism but displaced from its ideal position by constant offsets a', b', and c' as shown in figure 9. To determine them, we measured, for a fixed distance between the optical head and the target, the variations induced by small changes in the angles of the corner cube. From the results in figure 9, and by fitting them to the model described in [35], we obtained: $a' = 28.2$ µm, b' (along the measurement axis) $= 104.6$ µm, $c' = 51.5$ µm.

The constant b' does not have a significant impact, even though it lies along the direction of the measurement axis, because it is already included in the instrument offset. Only the changes induced by misalignments of the corner cube are relevant. In practice, with a sighting scope installed at the top of the corner cube, the target can be aligned with an angular reproducibility considerably better than 5°. Thus, the uncertainty contribution of the mechanical misalignments of the target on the measured distances was estimated to be 3 µm.

It should be pointed out that the mechanical errors of the target are small because, after an initial characterisation of the

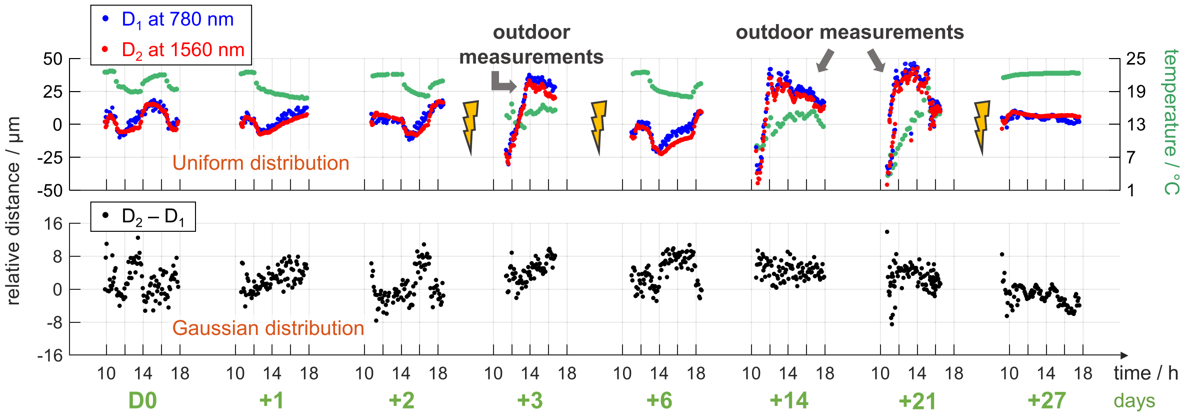

Figure 10. Above: results of a long-term measurement for each wavelength. Below: results for the distance difference between the two wavelengths. The lightning bolts represent the discontinuities in the curve that have been repaired, and the green curve at the top corresponds to the air temperature (vertical axis on the right).

gimbal mechanism, we adjust the axes of rotation and the position of the corner cube using micrometre screws. Certain error values, such as that of b', could be further minimized if more time were spent on adjustment.

3.2.8. Long-term drift.

The long-term mechanical changes, such as those due to the thermal expansion of the mechanical parts that compose the instrument, have also to be considered. To do this, a fixed distance of about 50 cm was measured over eight different days: during four consecutive days, then at +6, +14, +24 and +27 days after the start of the experiment. This fixed distance corresponds to the optical head and the target being mounted on the same aluminium breadboard, which was placed either in an air-conditioned laboratory (D0, D1, D2, D6 and D27) where the temperature can be modified by up to 5 °C, or outdoors (D3, D14 and D21) to reach lower temperatures. Thus, temperatures between 3.1 °C and 22.7 °C, atmospheric pressure between 994.4 hPa and 1020.7 hPa, and relative humidity between 19.1% and 74.3% were explored. The results are presented in figure 10 with a total of 699 measurements per wavelength, each being the average value over 10 packets of 75 points, equivalent to 12 s of measurement time.

Sometimes, between transport from the laboratory to outdoors, the measured distance changed by several hundred micrometres due to handling errors by the operator, which altered the mounting of the optical head and target on the breadboard. In the upper curve in figure 10, these measurement discontinuities have been repaired, but are still indicated by lightning bolts. Once corrected, the measured distances vary by no more than 90 µm peak-to-peak for a given wavelength.

This variation is the combination of several phenomena. First, there is the thermal expansion of the aluminium optical breadboard, about 21 µm m^{-1} $°\mathrm{C}^{-1}$, that is to say 210 µm over 50 cm and for the 20 °C of temperature variation of this experiment. Then, there is the thermal expansion of the instrument itself, which is the contribution that interests us. The instrument, also made of aluminium, has a mechanical offset of about 13 cm as shown in section 3.2.5. Thus, its thermal expansion should be about 55 µm for a temperature variation of 20 °C. Finally, the levelling of the head and target can change with time and temperature as explained in section 3.2.2. This can induce additive errors on the measured distances of up to 104 µm for the head and 87 µm for the target. The choice of not to manipulate the three levelling thumbscrews of the tribrachs throughout the experiment surely penalizes the results in figure 10, with levelling errors dominating the effects of thermal expansion. In other words, the experimental setup does not enable one to separate rigorously each contribution.

In the end, to take into account the thermal expansion of the instrument for potential temperature changes up to 30 °C, we consider mechanical changes up to 21 µm m^{-1} $°\mathrm{C}^{-1}$ × 0.13 m × 30 °C = 82 µm described by a uniform distribution, i.e. an uncertainty contribution of 24 µm.

Besides this, the difference of optical path lengths between the two wavelengths, $D_2 - D_1$, can be determined rigorously. Both distances are affected by the same mechanical changes (thermal expansion, levelling errors, but also operator-related measurement discontinuities), which thus cancel each other out. This difference is of great importance since in the calculation of the air-index compensated distance L it is multiplied by the factor A. As shown in figure 10, the difference varies by 22.4 µm peak-to-peak, with a standard deviation of only 3.7 µm. In addition, the corresponding distribution is close to a Gaussian.

3.2.8.1. Summary.

The mechanical sources of errors that must be considered for an absolute distance measurement at a single wavelength are summarized in table 2.

Table 2 summarizes the uncertainty contributions for the specific application presented at the beginning of section 3.2, in figure 5, where the distance is defined from the centres of the threads of the head and target tribrachs. This simple case only includes mechanical errors related to the instrument, not other contributions such as geometrical aspects linked to the application. For example, in a real-world application, the

Table 2. Summary of the uncertainty contributions due to the mechanics for a single wavelength.

			Uncertainty contribution	
Uncertainty component	Source of uncertainty	Distribution	Optical head	Target
$u_{\text{positionning}}$	Position reproducibility of the instruments on the Tribraches	Normal	5 µm	5 µm
$u_{\text{levelling}}$	Reproducibility of the vertical axis of the instruments	Uniform	$104\ \mu\text{m}/(2\times\sqrt{3}) = 30\ \mu\text{m}$	$87\ \mu\text{m}/(2\times\sqrt{3}) = 25\ \mu\text{m}$
u_{centring}	Difference between the vertical axis of the instruments and the reference mark	Normal	9 µm	15 µm
u_{offset}	Instrument offsets of-132.3221 mm (λ_1) and-132.3266 mm (λ_2)	Normal	25 µm	
u_{height}	Height difference between the EDM and the target	Cosine error	Negligible	
u_{gimbal}	Errors in the gimbal mechanisms (transit offset, beam offset, …)	Normal	2 µm	3 µm
$u_{\text{long-term drift}}$	Long-term effects (drifts due, for example, to thermal expansion)	Uniform	$(\text{offset} \times 21\ \mu\text{m m}^{-1}\ {}^{\circ}\text{C}^{-1} \times 30\ {}^{\circ}\text{C})/(2\times\sqrt{3}) = 24\ \mu\text{m}$	

measured distance might need to be reduce to a horizontal distance or be projected into a coordinate system, which implies knowledge of the height difference between the head and the target, as well as their geographical locations, all of which contribute to the uncertainty in the horizontal or projected distance.

3.3. Global uncertainty of the two-wavelength system

First, the uncertainty of the measurement at a single wavelength, D_i, was assessed by Monte-Carlo simulations considering all the sources of errors listed in tables 1 and 2. There are lot of mechanical contributions since many of them are counted twice, once for the optical head and once for the target, except the instrument offset and the long-term effects. Finally, for an SCR of 60 dB, the uncertainty is equal to 56.5 µm for distances up to 5 km, while for a degraded SCR of 50 dB, the result is similar with an uncertainty of 57.3 µm. In both cases, a Gaussian distribution is obtained as shown in figure 11.

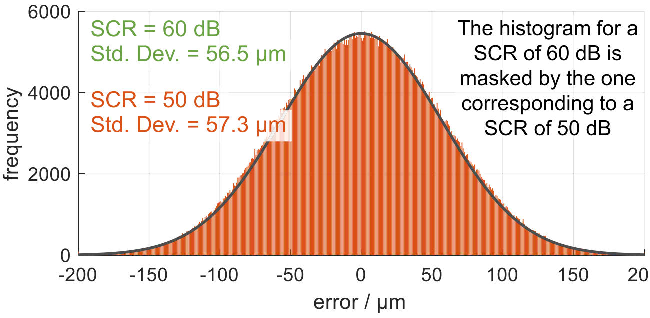

Figure 11. Error distribution for an optical path length measurement at 780 nm when both the telemetric and mechanical sources of errors are included. Monte-Carlo simulations provide similar results for measurements at 1560 nm.

Next, the uncertainty of the difference of optical path lengths between the two wavelengths, $D_2 - D_1$, was determined because this term is used in formula (5) for the calculation of the dispersion-based air-index compensated distance. Among the uncertainty contributions related to the ADM, amplitude-to-phase coupling and random noise observed at the phasemeter output are independent noises between the two wavelengths. On the contrary, the error in the value of the RF carrier is the same for both wavelengths, which induces a scale error only proportional to the difference of optical path lengths between the two wavelengths. As for crosstalk, as we shall see later, there is a phase dependency between the cyclic errors of the two wavelengths at a given distance. However, the phase shift between them evolves with the optical path delays caused by dispersion, and hence with the measured distance. For a set of random distances from 0 km to 5 km, all cases are possible. We therefore consider two independent crosstalk errors. The majority of the mechanical contributions are common to both distance measurements, such as positioning, centring, levelling, and misalignments in the gimbal mechanisms. The difference of instrument offsets between the two wavelengths must be quantified. In fact, it was determined in section 3.2.5, but also in section 3.2.8 simultaneously with the measurements of the long-term effects in figure 10 with an uncertainty of 3.7 µm. Thus, its uncertainty was not included since we already consider the long-term effects.

Finally, after Monte-Carlo simulations, the uncertainty in the difference between the two wavelengths, $D_2 - D_1$, is equal to 6.6 µm for an SCR of 60 dB, and 15.6 µm for one of 50 dB. The corresponding distributions are depicted in figure 12.

The dispersion-based air-index compensated distance can then be obtained applying the formula (5). We assume that the factor A is constant and equal to 48, with no uncertainty. In this case where only instrumental errors are included, the standard deviations in the compensated distance L are,

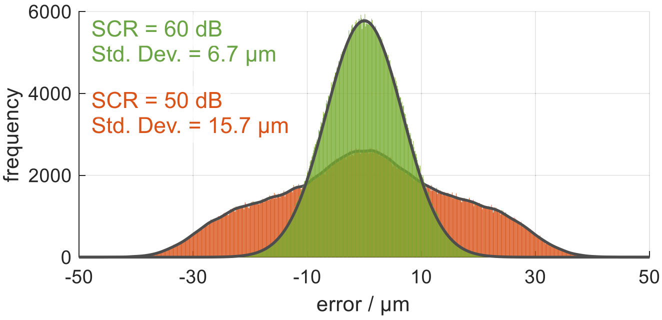

Figure 12. Error distribution for the optical path length difference between the two wavelengths when both the telemetric and mechanical sources of errors are considered. The results from the Monte-Carlo simulations, which highly depend on the SCR, were obtained for a general case where the cyclic errors at 780 nm and 1560 nm are uncorrelated.

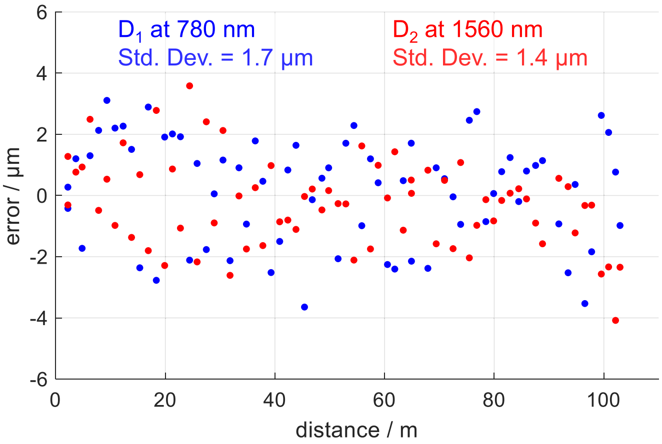

Figure 13. Difference between the measurements of the interferometer and those of the EDM for each wavelength. The air refractive indices were calculated using Ciddor's equation.

respectively, 323 µm and 752 µm for SCRs of 60 dB and 50 dB. Over 5 km, they correspond to relative uncertainties of 0.07 ppm and 0.15 ppm, respectively. Finally, the related distributions are similar to those in figure 12, but 48 times wider. This highlights the need to optimise the power of the received signals: with an SCR degraded by 10 dB, the uncertainty doubles, and the Gaussian error distribution turns into something closer to a triangle. In the current system, crosstalk is the main source of uncertainty without which the uncertainty of the instrument would be only 230 µm ($k = 1$).

We should stress that the above results are an approximation based on the case of dry air. In the general case, i.e. that of moist air, humidity must be taken into account. When the group index is used for wavelengths of 780 nm and 1560 nm, p_ω has to be measured with an accuracy better than 200 Pa if we want to reach an accuracy of 1 mm in a distance measurement of 5 km. This humidity can be determined either by using a source at a third wavelength, preferably a microwave one [21], or more simply by sampling the atmosphere with environmental sensors. In this latter case, where standard hygrometers indicate relative humidities, values better than 15.0% at 10 °C or 7.5% at 20 °C are required. To achieve this, at least two humidity measurements must be made, i.e. one at each end of the baseline. If the terrain is supposed uniform, a bold assumption for a path of several kilometres, one can apply a simple model where water vapour pressure decreases with altitude [36]. Currently, the humidity measurement and the estimation of its uncertainty remain a challenge, especially when it is determined by sampling the atmosphere with environmental sensors. The uncertainty in the air-index compensated distance only includes the contributions listed in tables 1 and 2, not that of the humidity measurement. It follows that the uncertainty values given above are necessarily optimistic.

4. Validation of the two-wavelength EDM

4.1. Comparison with a 50 m-long interferometric bench

The performance of the instrument developed was first compared with that of a 50 m-long interferometric bench, in a controlled indoor environment. The beams at 780 nm and 1560 nm were propagated over 100 m using a double round trip approach. To validate measurements performed at each wavelength, the interferometric distance was corrected by the phase refractive index for a wavelength at 633 nm then multiplied by a factor of two, while the two distances measured by the EDM were corrected by the group refractive index of air for wavelengths of 780 nm and 1560 nm. The result of the comparison is presented in figure 13 where each distance measured by the EDM is an average over five packets of 75 points.

The standard deviations observed in the differences between the distance provided by the interferometer and those measured by the EDM are 1.7 µm and 1.4 µm for, respectively, wavelengths of 780 nm and 1560 nm. The performances are limited by crosstalk as shown in figure 14, with cyclic errors of amplitudes of 2.5 µm at 780 nm and 1.0 µm at 1560 nm. According to formula (9), this corresponds to SCRs of 65.5 dB and 73.5 dB, respectively. In addition, sinusoidal curves fit well the experimental points, with standard deviations of residuals of only 0.4 µm and 1.0 µm.

In the case of displacement measurements, only the uncertainty contributions of the telemetric part need be considered. The errors obtained in this experiment are slightly smaller than those estimated in section 3.1. Because over such short distances the received RF signals are higher and the SCR above 60 dB for both wavelengths. In addition, each value was averaged over 6 s.

From these results, we can calculate the air-index compensated distance. To do this, we used the dispersion-based

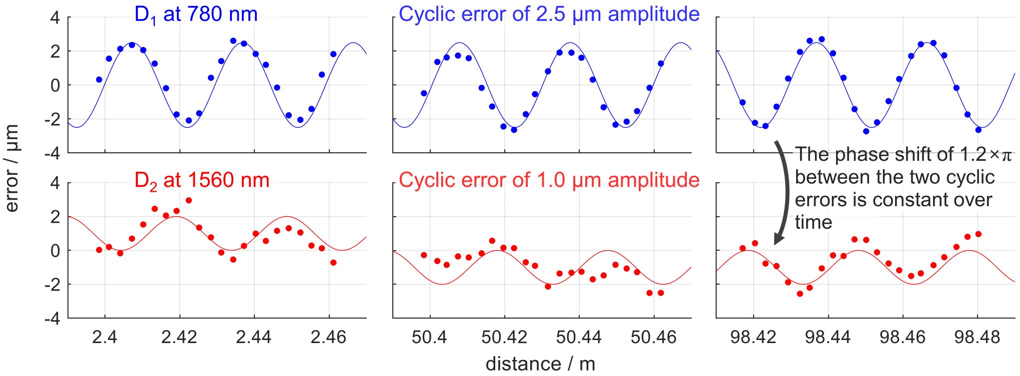

Figure 14. Close-up view of the cyclic errors of the EDM at each wavelength due to crosstalk.

model in formula (2) with the Voronin and Zheltikov equation [17]. The latter defines the air refractive index for a wide range of wavelengths, including infrared at 780 nm and 1560 nm.

As explained previously, the case of dry air is a good approximation of the general case. Thus, with a factor A of 48, the standard deviation of the compensated distance should be about 48 times higher than that of the distance difference between the two wavelengths. In our case, the two cyclic errors have a phase shift between their sine curves of 1.2 π. Because of the air refractive index dispersion, this phase shift is expected to change with the measured distance. Indeed, the optical path length covered by the 780 nm beam is about 6 mm per kilometre shorter than that covered by the one at 1560 nm, while the phases of the crosstalk signals remain constant for each wavelength. The phase shift between the cyclic errors of the two wavelengths, $\phi_{\Delta n}$, i.e. the dispersion of the cyclic errors, can be written as:

$$\phi_{\Delta n}(L,T,p,x,p_\omega) = \phi_{\Delta n}(L=0) + 4\pi \times \Delta n(T,p,x,p_\omega) \times L \times \frac{f_{RF}}{c} \quad (13)$$

where $\phi_{\Delta n}(L=0)$ is the dispersion of the cyclic errors measured at small distance, i.e. 1.2 π as depicted in figure 14, and Δn is the dispersion between the two wavelengths of our system, i.e. 780 nm and 1560 nm, which depends on the environmental parameters and is equal to 5.7 mm km^{-1} for an air temperature of 20 °C, an atmospheric pressure of 1013.25 hPa, a relative humidity of 50%, and a CO_2 content of 400 ppm.

For each wavelength, the crosstalk comes mainly from the imperfect isolation of the optical beam splitter that acts as circulator. Thus, one part of the signal (the crosstalk) is detected directly by the phasemeter, while the other (the measurement signal) travels a few metres more through the optical fibres (~2 m) before emerging into free space in the direction of the target. The phase shift between the crosstalk and the measurement signal, and thus the cyclic error observed in the measured distances, depends on the phase acquired by the measurement signal when it propagates through the air, and hence on the air refractive index, as shown in formula (8). The cyclic errors in figure 14 have periods equal to half the synthetic wavelength $c/(n \times f_{\mathrm{RF}})$, where n a function of the vacuum optical wavelength λ, the air temperature T, the pressure p, the partial pressure of water p_ω, and the CO_2 content x. As a consequence, the phase shift between the cyclic errors in figure 14, $\phi\Delta n$, depends on the dispersion $\Delta n = n_1 - n_2$ between the two wavelengths, which is described by formula (13). The value of $\phi\Delta n(L=0)$ depends on the optical path differences through the optical fibres for each wavelength.

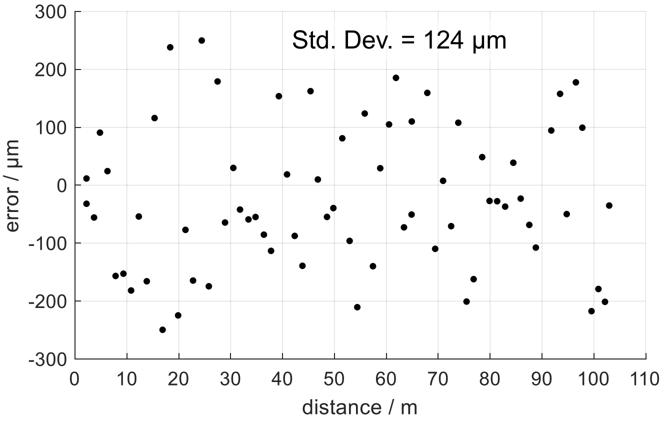

Figure 15. Difference between the interferometric distance and the air-index compensated distance.

Finally, because the cyclic errors are almost π out of phase, the standard deviation of the distance difference in figure 13 is 2.6 µm. The uncertainty in the compensated distance should therefore be around 48 × 2.6 µm = 124.8 µm. The result presented in figure 15, obtained by applying formula (2) with the data in figure 13, lies in excellent agreement with this estimate.

Figure 16 shows the details of the measurements of the air-index compensated distance around 2 m, 50 m and 98 m. We observe the presence of a cyclic error with an amplitude of 200 µm, which is compatible with the standard deviation of 124 µm measured in figure 15. Crosstalk is therefore the parameter that contributes the most to the uncertainty of the instrument. In figure 16, the fit of the experimental points is not perfect, probably because the level of crosstalk varies slightly over time. The residuals have a standard deviation of 63.1 µm.

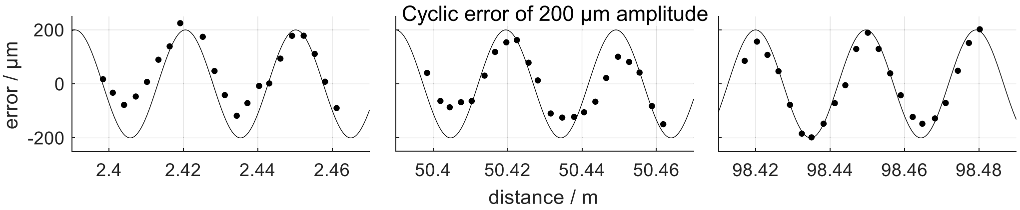

Figure 16. Close-up view of the cyclic errors in the air-index compensated distance. This curve was obtained from the data shown in figure 14.

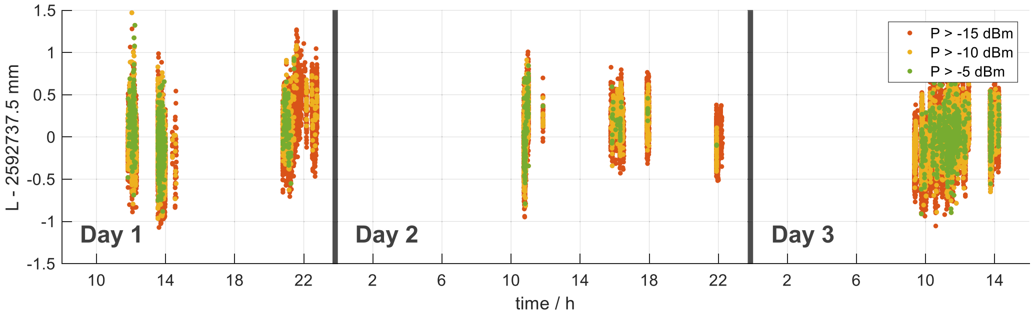

Figure 17. Air-index compensated distance measurement over 2.6 km as a function of the received RF power. Points of received powers lower than −15 dBm have been removed. The green dots correspond to SCRs above 60 dB, while the orange dots correspond to SCRs above 50 dB.

4.2. Distance measurement over 2.6 km

4.2.1. Long-term measurement. A long-term measurement was performed during three successive days, from Tuesday 20 to Thursday 22 September 2022. This was performed in the co-location site of the Observatoire de la Côte d'Azur located on the Plateau de Calern, close to Grasse (France). The instrument was set up inside the building of the MEO station, while the target was installed 2.6 km away, at 156 m above in the mountain. During this experiment, the sky was variable, from slightly overcast to heavily overcast, which avoided exposure to sunlight and so to strong air turbulences. The temperature ranged between 10 °C and 18 °C, the pressure between 871 hPa and 879 hPa, and the relative humidity between 40% and 90%.

The long-term measurement is presented in figure 17. The average distance over 3 days equals to 2592 737.5 mm for the experimental points in green, which correspond to received RF power higher than −5 dBm. In such a case, the SCR is higher than 60 dB for each wavelength. Indeed, the crosstalk levels can be determined experimentally by measuring the power of the RF signals received at the photodiode outputs when the optical beams are masked: they are typically around −65 dBm.

The optical head and the target were left in place throughout the entire measurement. However, the levelling of the head and its aiming were adjusted whenever necessary, so, the errors of the head due to its levelling and the gimbal misalignments still need to be taken into account, as well as one of the main sources of uncertainty, namely the long-term drifts. The predicted stability, obtained by a Monte-Carlo simulation including the contributions of the mechanical errors of the optical head, is equal to 320 µm.

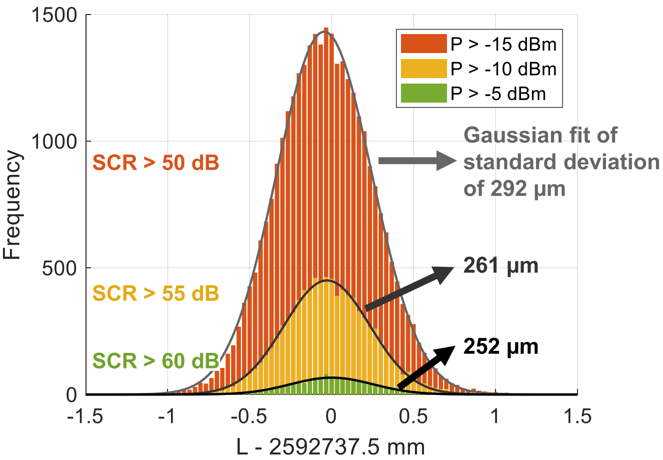

Figure 18. Distributions of the air-index compensated distances measured over 2.6 km, for 3 days, as a function of the received RF power.

Finally, as shown in figure 18, Gaussian distributions with standard deviations less than 292 µm were obtained experimentally at any received power down to −15 dBm. This is very close to the result of the Monte Carlo simulation. An air-index compensation at such a level means that the measurements of the optical path lengths at 780 nm and 1550 nm were highly resolved, 48 times lower than 292 µm, i.e. 6.1 µm. The experimental results obtained over a temperature range up to 8 °C and a pressure range up to 8 hPa confirm that the two-wavelength ADM works well and is able to compensate for the air refractive index.

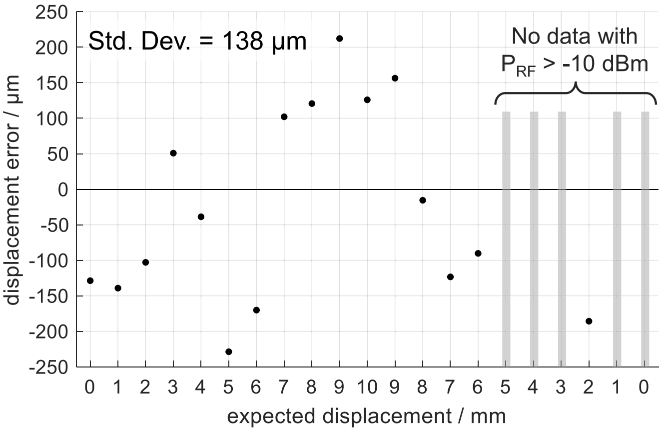

Figure 19. Displacement measured at 2.6 km using the dispersion-based air-index compensation technique.

According to the formula (13), the cyclic errors of the two wavelengths are nearly in phase after propagation over 2.6 km in the environmental conditions of this experiment, i.e. temperature around 14 °C, pressure around 875 hPa, and relative humidity around 65%. This is a favourable case that minimizes the impact of the crosstalk on the optical path length difference $D_2 - D_1$ and explains why an arcsine distribution typical of a cyclic error is not manifest in figure 18, even for a low SCR close to 50 dB as in the orange histogram. The results obtained in figure 18 thus show no power dependency.

4.2.2. Displacement measurements. In order to confirm the absence of cyclic error for the specific distance of 2.6 km, the distant target was mounted on a translation stage and displaced by steps of 1 mm, from 0 mm to 10 mm and back again, at rate of 1 mm min^{-1}. We selected only data with RF powers higher than -10 dBm (SCR $>$ 55 dB) since the weather conditions at the time of the experiment did not allow us a better selection. During the 20 min it took to make the measurement, the alignment of the optical head remained unchanged, but atmospheric conditions varied, which modified the alignment of the beam and lowered the received RF signal. Consequently, some distance values are missing, as visible in figure 19.

The comparison between the measured displacement and the displacement applied to the translation stage is depicted in figure 19. The difference between the two, called the displacement error, has a standard deviation of 138 µm and a maximum error of 230 µm. As anticipated in figure 18 where no arcsine contribution is visible in the distance distributions, there is no observable cyclic error. However, as we shall see in the next section, for other distance values, the cyclic errors obtained for each wavelength might not necessarily compensate each other, and hence a cyclic error in the compensated distance might arise.

The uncertainty in the two-wavelength EDM for displacement measurements is therefore roughly 140 µm ($k = 1$) for a distance around 2.6 km.

4.3. Distance measurement over 5.4 km

4.3.1. Long-term measurement. The previous experiment was repeated over a distance twice as large, and a period twice as long. It was performed between Wednesday 12 and Monday 17 October 2022. The two-wavelength EDM was placed on a concrete pillar on the rooftop of the Laboratoire National de métrologie et d'Essais (LNE) building (Paris, France), 22 m above the ground, while the target was located 5.4 km away at the Meudon observatory (Meudon, France), at ground level and about 75 m above the instrument.

Over the 5 days of measurement, the temperature ranged between 14 °C and 24 °C, the pressure between 998 hPa and 1015 hPa, and the relative humidity between 35% and 95%. The received RF powers varied according to the visibility and atmospheric perturbations. On the first day, the weather was variable with a clear sky in the morning, followed by a slightly overcast sky from noon onwards. The next day was very overcast, measurements being made only between 10 a.m. and 2 p.m. when there was no rain. On a positive note, the absence of sunshine during this short period resulted in a very stable received power with many points of RF powers above -5 dBm, i.e. with an SCR higher than 60 dB. By contrast, in the afternoon of day 2, as well as on day 3 and in the morning of day 4, the visibility was very poor with rain and humidity near 90%. In the afternoon of day 4, the sky cleared up and only a light cloud cover persisted. On day 5 (Sunday), no measurement was performed. On the last day, the sky was overcast, and a light rain perturbed the measurements slightly.

As shown in figure 20 for SCRs higher than 60 dB (in green), the average distance is 5416 244.2 mm with a standard deviation of 276 µm. As discussed above in section 4.2.1, the expected stability for such a case was 320 µm ($k = 1$). Moreover, in figure 21, the histogram of these distances measured over 5 days could be fitted to a Gaussian curve with a standard deviation of only 185 µm.

In the environmental conditions of this experiment, and according to the formula (5) for a distance of 5.4 km, the cyclic errors for measurements at 780 nm and 1560 nm due to crosstalk are phase-shifted by almost π, and so add up in optical path length difference $D_2 - D_1$. In this unfavourable case, when the received RF power is less than -5 dBm, the results are greatly affected by crosstalk. With temperature and pressure changes of 10 °C and 17 hPa over the 5 days of measurement, the optical path lengths varied by one synthetic wavelength as shown in figure 22, while the phases of the crosstalk signals resulting from the poor isolations of the optical splitters acting as circulators remained constant. Thus, all possible values of the cyclic errors were obtained. Naturally, this impacts the air-index compensated distance. As shown in figure 21, the distance distributions for low received RF powers exhibit a double peak, which is typical of a cyclic error dominating the other contributions (see figure 4). However, this double peak is not perfectly symmetrical because we measured more points for certain phases (or certain optical path lengths). In other words, the measured phases unevenly distributed.

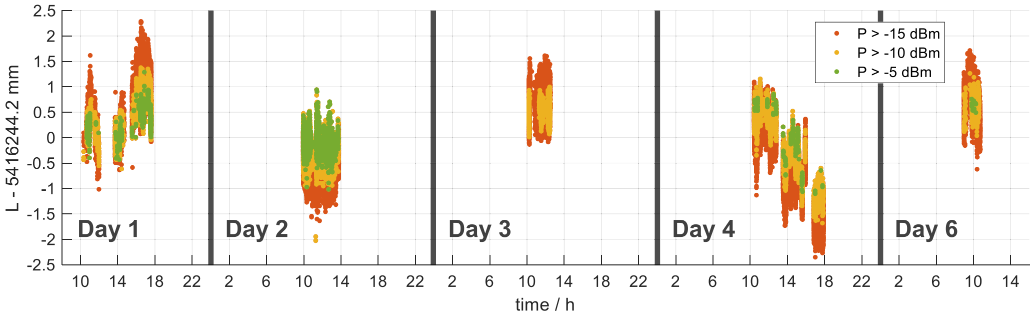

Figure 20. Air-index compensated distance measurement over 5.4 km as a function of the received RF power. The green dots correspond to SCRs above 60 dB, and the orange ones to SCRs above 50 dB.

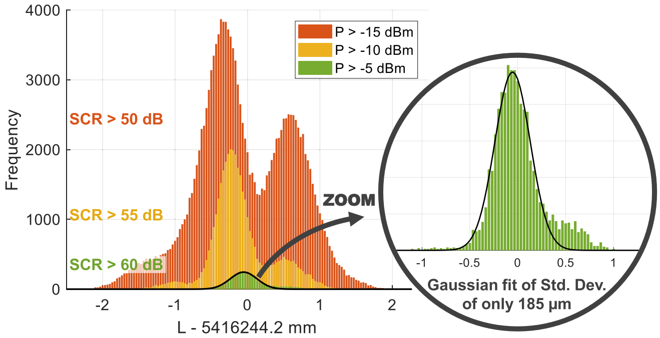

Figure 21. Distributions of the air-index compensated distances measured over 5.4 km and 6 days as a function of the received RF power.

About 148 000 points were measured with RF powers down to −15 dBm. To determine the distance from these points, we can either take the average value, or else adopt a statistical approach by fitting the theoretical distribution of these points to the experimental histogram coloured in orange in figure 21. As explained above, the theoretical distribution is expected to have a symmetrical double-peaked shape, with the central value being the true value, but only if the measured optical path lengths in figure 22 are uniformly distributed in phase between 0 and 2π. Given the large number of measurements, it was possible to correct the experimental distribution so as always to have the same number of points measured for a given phase range. To this end, as shown figure 22, for all the optical path lengths measured at 780 nm, we counted the number of points equal to a given phase, modulo 2π and $\pm 2\pi/600$ rad, which corresponds to a range of about ±50 µm. After this, some of the measured optical path lengths were randomly removed to yield a set of 500 points for each measured phase range (each time we removed a measurement at 780 nm, we also removed the corresponding one at 1560 nm). In this way, the distribution of the air-index compensated distances was rearranged using a uniform representation of the measured phases. The resulting curve shown on the right-hand side of figure 23 now has a symmetrical double peak.

In parallel, we ran a Monte-Carlo simulation to assess the uncertainty of the air-index compensated distance for the specific case of a distance of 5.4 km, i.e. when the cyclic errors for 780 nm and 1560 nm have a phase shift of 1.3 π. However, only the telemetric contributions were considered, not the mechanical ones (levelling, gimbal misalignments and long-term drifts). Thus, if we consider SCRs of 57 dB for both wavelengths, a distribution close to the experimental one is obtained. As shown in figure 23, the tails and peaks of the experimental distribution are actually broader, probably because of the mechanical errors, but also because the SCRs vary over time. In the end, it is possible to determine the value of the compensated distance as the central value of the distribution, namely 5416 244.3 km. This value lies only 0.1 mm away from the central value of the Gaussian curve obtained for SCRs higher than 60 dB. This demonstrates that when SCRs are low (e.g. 50 dB), the same result can be obtained as for high SCRs (e.g. higher than 60 dB), albeit at the expense of a long-term measurement and more complex data processing. However, this approach works because the measured distance was stable over the measurement period of 6 days. This approach is thus based on a strong initial assumption that the measured distance is stable, which is the case here. In a real-world application, however, where distance changes may occur over time, for example in landslide monitoring, such an approach would not be possible. In the next section, an alternative solution whereby measurements need only be performed over a short time is presented.

For distances of 5.4 km or 2.6 km, we observed no changes in the measured distances at the scale of a few hundred micrometres. Yet, for measurements over several days, we would have expected potential changes in the radius of curvature of the optical beams along the measurement path, the so-called second velocity correction [37]. Moreover, the dispersion of light and its changes with temperature and pressure did not significantly affect the trajectory of one beam relative to the other, and thus the difference in optical path lengths.

The absence of drift at the scale of a few hundred micrometres also shows that the humidity measurements performed in these campaigns were highly representative of the overall humidity variations along these two baselines. For practical reasons, the humidity values used for each of these experiments were those recorded at the head end only (no recording was made at the target end) using a Vaisala PTU300 sensor, which provides the temperature at ±0.2 °C and the relative

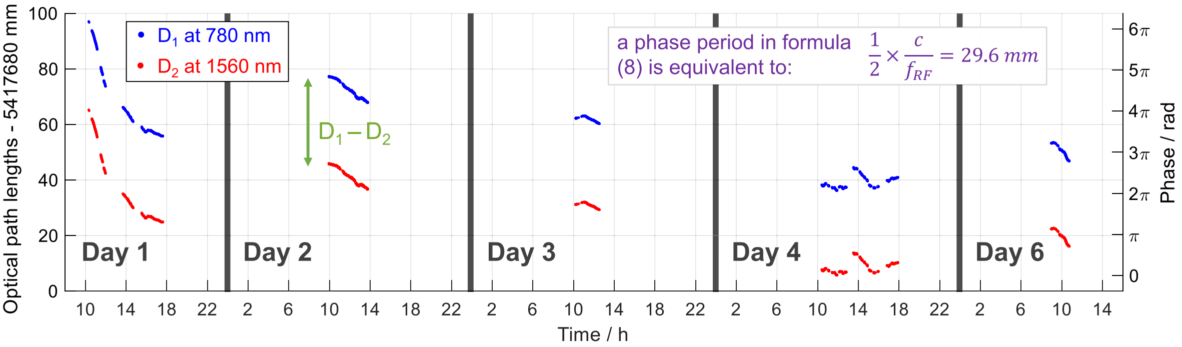

Figure 22. The optical path lengths that were measured for the determination of the air-index compensated distance.

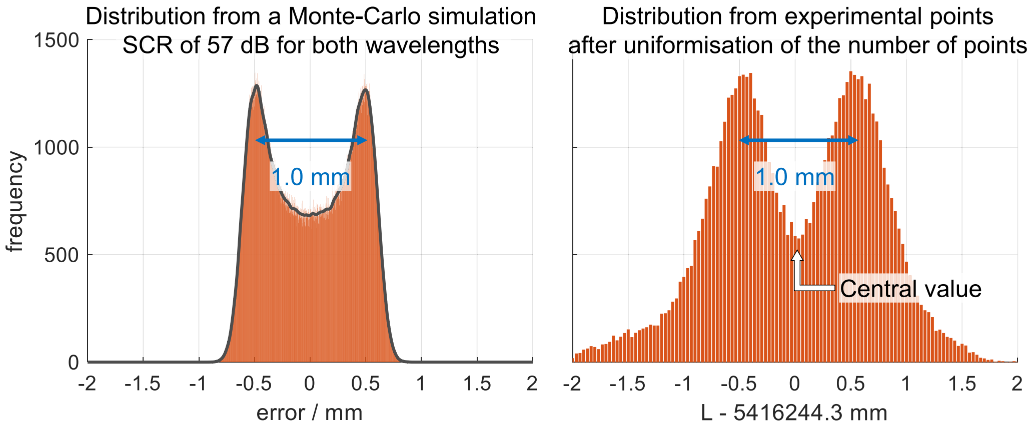

Figure 23. Comparison of the simulated and experimental distributions of the air-index compensated distances measured over 5.4 km as for a received RF power as low as −15 dBm and considering only the telemetric contributions.

humidity at ±1%. There was probably an offset between a humidity measured at the head side and the humidity integrated over a whole baseline, but the humidity variations were well tracked by this single-point measurement. This was true over 2.6 km, in a rocky mountain environment, as well as over 5.4 km, in a highly built-up urban environment. To give an order of magnitude of the achievable level of tracking of the humidity variation, an error of 60 Pa in the measured partial pressure of water would produce an error of about 0.3 mm over an air-compensated distance of 5.0 km.

Next, it should be noted that one source of error has not been taken into account, namely the stability of the pillars and tripods used for the long-term measurements. Tripods were used in most cases, except for the measurement over 5.4 km where the head was mounted on a concrete pillar. Just like our instruments, they were protected from the sun as well as possible using parasols. In future, studies need to be carried out to guarantee the long-term stability of the pillars and tripods, and quantify their potential movement due to bending, tilting, or thermal expansion. However, the results presented in this article suggest that their stability was sufficient, at least for up to 6 days.

Lastly, thanks to the measurements shown in figures 20 and 22, it is possible to extract a value for the integrated group refractive index of the air along the path for each wavelength. These indices equal to the ratio between optical path lengths in figure 22 and the air-index compensated distance in figure 20, range from 1.000 266 to 1.000 283.

4.3.2. *Displacement measurements.*

In the same way as for the experiment over 2.6 km, the distant target was mounted on a translation stage on the final day of measurement. It was displaced over an entire synthetic wavelength (3 cm), to reveal any potential cyclic errors. To do this, steps of 1 mm were applied every minute to produce a displacement from 0 mm to 30 mm, but unlike the experiment over 2.6 km, with no return to the initial position.

During this measurement, owing to poor visibility, signals including those with RF powers as low as −15 dBm were processed. Thus, the SCR was close to 50 dB for both wavelengths. In practice, this value varies over time due to atmospheric turbulence. Nevertheless, if we assume an SCR of 52 dB for each wavelength, the amplitude of their cyclic error will be 11.8 μm. As we saw earlier, these errors add to each other for a distance of 5.4 km due to the phase shift of 1.3π, so the distance difference between them will have a cyclic error of amplitude 21.1 μm. Multiplying this error by the factor A of 48 will thus cause a cyclic error of 1 mm amplitude in the air-index compensated distance. The difference between

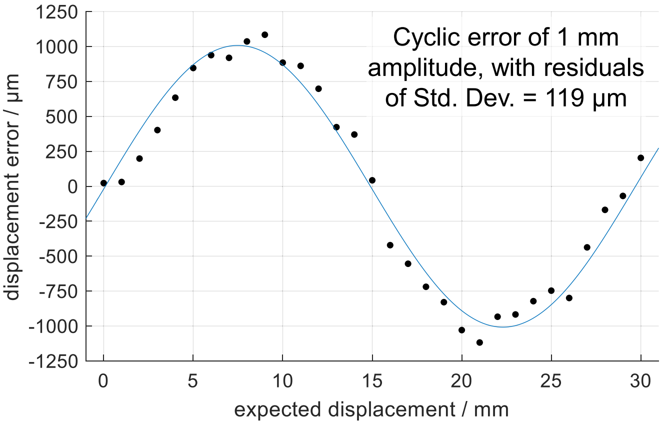

Figure 24. Displacement measured at 5.4 km with the dispersion-based air-index compensation technique.

the measured displacement and that applied to the translation, presented in figure 24, lies in very good agreement with this estimate.

Finally, a sine curve was fitted to the experimental points, which yielded in a sinusoid of amplitude 1 mm and a standard deviation of the residuals of only 119 µm. This value corresponds to the accuracy of the two-wavelength EDM for a displacement measurement over 5.4 km in the absence of crosstalk. The resolution of the system obtained for a single wavelength is thus 48 times better, i.e. only a few micrometres. The distributions of the optical path lengths at 780 nm and 1560 nm corresponding to this experiment, of standard deviations around 5 µm over 1 min despite atmospheric turbulences, were presented as preliminary results in [38].

Note that moving the distant target over a synthetic wavelength using a translation stage allows one to characterize the crosstalk-related cyclic error, and so remove it (for this purpose the translation stage should form part of the mechanical structure of the target, and the instrument offset should be determined for the zero graduation of the stage). This correction can be made with an uncertainty at the level of the residuals of the fitted sine curve, i.e. with a standard deviation of 120 µm as shown in figure 24. In other words, this procedure makes it possible to achieve almost the same uncertainty as that of an instrument free of crosstalk, i.e. 230 µm ($k = 1$).

5. Discussion and conclusion

When traditional EDMs are used, the air refractive index must be known, and hence the environmental parameters used to calculate it from semi-empirical formulas, i.e. the air temperature, the atmospheric pressure, the humidity and the CO_2 content. For measurements over long distances (e.g. several kilometres), however, merely sampling the atmosphere using weather sensors is both impractical and insufficient to provide an accurate enough value for the air refractive index. Indeed, it is extremely difficult to integrate the spatial and temporal variations of the air index along an optical path. In this case, real-time inline refractivity compensation can be applied by simultaneously measuring two optical path lengths with two different wavelengths and applying a dispersion relation. In this paper, an EDM based on this principle, and operating at 780 nm and 1560 nm, was presented. It is based on the phase measurements of light sources intensity-modulated by a RF at 5 GHz, the value of this RF carrier providing a direct link to the SI definition of the metre.

The choice of these wavelengths induces a large factor A of 48, which degrades the uncertainty on the dispersion-based air-index compensated distance. In fact, the optical path lengths must be measured with an uncertainty better than 20 µm to reach a final standard uncertainty below 1 mm for a distance of 5 km. However, such wavelengths enable the used of fibre-guided optical components and lead to a more robust and compact instrument than one based on free-space optics, that is much easier to use in the field.

The two-wavelength EDM was fully characterised, and an uncertainty budget established. Firstly, the uncertainty of the telemetric system itself (i.e. with no mechanical errors) was assessed to 4 µm for measurements of optical path lengths up to 5 km. Among the different sources of errors identified, crosstalk is the parameter that contributes the most to the uncertainty of the telemetric system. It induces a cyclic error that depends on the received powers, and hence on atmospheric visibility. In practice, under favourable atmospheric conditions, an SCR of more than 60 dB can be obtained for each wavelength, which corresponds to an uncertainty contribution of 3.3 µm in the measurement of an optical path length. However, the contribution for the air-index compensated distance depends on the phase shift between the cyclic errors obtained at each wavelength. In fact, these cyclic errors can either add up or cancel out depending on this phase shift. The phase shift between the cyclic errors evolves with the dispersion and therefore depends periodically on the distance to be measured, with a spatial period of about 5.1 km for a temperature of 20 °C and a pressure of 1013.25 hPa.

In order to state the uncertainty for absolute distance measurements, the mechanical sources of errors were also considered. In this paper, seven sources of mechanical error were identified, including long-term changes due mainly to thermal effects. Thus, considering all the uncertainty contributions, telemetric and mechanic, uncertainties of 323 µm and 752 µm ($k = 1$) in the compensated distance were estimated for, respectively, SCRs of 60 dB and 50 dB. These values were obtained using Monte-Carlo simulations, in which the phase shift between the cyclic errors obtained for each wavelength is assumed to be independent. This is therefore a general case that applies to measurements of any distance between 0 km and 5 km, without a specific crosstalk treatment for a given distance.

The ability of the EDM developed to compensate for air refractive index variations was tested by measuring fixed distances of 2.6 km and 5.4 km outdoors over several days, where temperature variations could be up to 10 °C and pressure variations up to 17 hPa. Standard deviations on the measured distances of, respectively, 252 µm over 3 days and 185 µm over 6 days were obtained. These results demonstrate that the two-wavelength system enables refractivity compensation along the optical wave paths at better than 250 µm.

The performance of the system was checked by measuring its accuracy for displacement measurements. For this purpose, the distant target was displaced by small steps over distances of a few centimetres. A first validation was performed for distances up to 100 m by comparison with a 50 m-long indoor interferometric bench, in a controlled atmosphere. The standard deviation in the difference between the compensated distance and the interferometer was 124 µm. Then, for a target located 2.6 km away, a standard deviation of 138 µm was obtained for a displacement of 1 cm in steps of 1 mm. The accuracy depends very much on the SCR, which must be greater than 60 dB. Thus, for measurements over 5.4 km, with a low received power and an SCR close to 50 dB, there appeared in the air-index compensated distance a cyclic error of amplitude 1 mm.

Lastly, it was shown that we could deal with the effect of the crosstalk, and thereby improve uncertainties. When the crosstalk effect is very pronounced, for instance when the cyclic errors at each wavelength add to each other, and when the atmospheric conditions vary sufficiently during the measurement campaign to change the optical path lengths by more than half a synthetic wavelength, the distribution of the measured compensated distance displays a double-peaked shape typical of an arcsine distribution. As demonstrated experimentally for a distance of 5.4 km, the central value of this symmetrical distribution differed by only 0.1 mm from that obtained with a crosstalk level reduced by 10 dB, which had a Gaussian distribution. Thus, even for an unfavourable crosstalk configuration, measurement biases related to a cyclic error can be corrected by studying the distribution of the measured distances. However, this requires a measurement over a long period, with for example temperature variations of the order of 6 °C for a distance of 5 km and a synthetic half-wavelength of 29.6 mm (corresponding to a modulation frequency around 5 GHz).

Another way to address crosstalk is to move either the distant target, or the optical head, by more than half a synthetic wavelength. The resolution of our two-wavelength EDM allows us to quantify the cyclic error with an uncertainty of the order of 0.1 mm and thus to remove it using a sine curve fitting. This technique was tested successfully for a distance of 5.4 km where the crosstalk induced a cyclic error of 1 mm peak-to-peak amplitude. After correction for this error, a residual of standard deviation of only 119 µm was obtained.

We have demonstrated in this paper that the two-wavelength EDM developed achieves a resolution close to 120 µm in a range from 0 km to 5.4 km. Moreover, in measurement campaigns lasting several days with significant meteorological changes, a measurement stability better than 250 µm was observed for distances of up to 5.4 km.

The reader must bear in mind that the results presented in this paper only consider the instrumental uncertainty. Thus, to go further in the uncertainty assessment of absolute distance measurements, a specific study of the uncertainty of formula (2) that provides the dispersion-based air-index compensated distance should be performed for the wavelengths of our system. Provided such data are available, the work presented here shows that an absolute distance measurement up to 5 km with a relative uncertainty better that 10^{-7} would be achievable with a compact and transportable instrument of similar design. However, the uncertainty for absolute distance measurements will have to be confirmed by comparison with a reference baseline such as the 864 m-long Nummela Standard Baseline [39].

Data availability statement

The data cannot be made publicly available upon publication because they are not available in a format that is sufficiently accessible or reusable by other researchers. The data that support the findings of this study are available upon reasonable request from the authors.

Acknowledgments

The authors are very grateful to J Cali from *École Supérieure des Géomètres et Topographes* (ESGT, France) for the availability of their interferometric bench and of their laser tracker Leica AT401. The authors would also like to thank C Courde and colleagues from *Observatoire de la Côte d'Azur* (OCA, France) for their hospitality and help with the measurements over 2.6 km. The authors also thank D Pesce from *Institut national de l'information géographique et forestière* (IGN, France) for assistance and advice during the measurement campaigns, and O Martin from IGN for the design and construction of RF amplifiers. Lastly, the authors would like to thank their colleague M D Plimmer from *Conservatoire National des Arts et Métiers* (Cnam, France) for proofreading the article, which helped to improve the quality of the English.

This work was partially funded by the Joint Research Project (JRP) 18SIB01 GeoMetre. This project has received funding from the European Metrology Programme for Innovation and Research (EMPIR, funder ID 10.13039/100014132), co-financed by the participating states and from the European Union's Horizon 2020 research and innovation programme.

ORCID iD

Joffray Guillory https://orcid.org/0000-0002-0325-1695

References

[1] Cosser E, Roberts G, Meng X and Dodson A 2003 Measuring the dynamic deformation of bridges using a total station *Proc. 11th Fédération Int.e Des Géomètres (FIG), Symp. on Deformation Measurements (Santorini, Greece)* (available at: www.fig.net/resources/proceedings/2003/santorini_comm6/I-Monitoring%20Static%20and%20Dyn/I9.pdf)

[2] García-Asenjo L, Martínez L, Baselga S, Garrigues P and Luján R 2023 Design, establishment, analysis, and quality control of a high precision reference frame in Cortes de Pallás (Spain) *Appl. Geomatics* **15** 359–70

[3] Curtis C J 1992 Calibration and use of the mekometer ME5000 in the survey of the channel tunnel *Proc.*

Workshop on the Use and Calibration of the Kern ME5000 Mekometer, Stanford Linear Accelerator Center, Stanford University (Stanford, CA, USA) pp 67–82

[4] Frukacz M, Presl R, Wieser A and Favot D 2016 Pushing the sensitivity limits of TPS-based continuous deformation monitoring of an alpine valley *Proc. 3rd Joint Int. Symp. on Deformation Monitoring (JISDM)* (*Vienna, Austria*)

[5] USGS Earthquake Hazards Program Two-color electronic distance meter (EDM) (available at: https://earthquake.usgs.gov/monitoring/deformation/edm/)

[6] Langbein J O, Linker M F, McGarr A F and Slater L E 1987 Precision of two-color geodimeter measurements: results from 15 months of observations *J. Geophys. Res.* **92** 11.644–11.656

[7] Gervaise J 1983 First results of the geodetic measurements carried out with the Terrameter, two wavelength electronic distance measurement instrument *Proc. Geodätischen Seminar Über Electrooptische Präzisionsstreckenmessung (Munich, Germany)* pp 213–29

[8] Wezka K, García-Asenjo L, Próchniewicz D, Baselga S, Szpunar R, Garrigues P, Walo J and Luján R 2022 EDM-GNSS distance comparison at the EURO5000 calibration baseline: preliminary results *J. Appl. Geod.* **17** 101–9

[9] Koivula H, Häkli P, Jokela J, Buga A and Putrimas R 2012 GPS metrology–bringing traceable scale to local crustal deformation GPS network *Geodesy for Planet Earth International Association of Geodesy Symposia* vol 136, ed S Kenyon, M Pacino and U Marti (Springer)

[10] García-Asenjo L, Baselga S, Atkins C and Garrigues P 2021 Development of a submillimetric GNSS-based distance meter for length metrology *Sensors* **21** 1145

[11] Baselga S, García-Asenjo L, Garrigues P and Luján R 2022 GBDM+: an improved methodology for a GNSS-based distance meter *Meas. Sci. Technol.* **33** 085020

[12] Edlén B 1966 The refractive index of air *Metrologia* **2** 71–80

[13] Bönsch G and Potulski E 1998 Measurement of the refractive index of air and comparison with modified Edlén's formulae *Metrologia* **35** 133–9

[14] Ciddor P E 1996 Refractive index of air: new equations for the visible and near infrared *Appl. Opt.* **35** 1566–73

[15] Ciddor P E and Hill R J 1999 Refractive index of air. 2. Group index *Appl. Opt.* **38** 1663–7

[16] International Association of Geodesy (IAG) 1999 Resolutions adopted at the XXIIth general assembly in Birmingham (available at: https://office.iag-aig.org/doc/5d7b8fda0c032.pdf)

[17] Voronin A A and Zheltikov A M 2017 The generalized Sellmeier equation for air *Sci. Rep.* **7** 46111

[18] Owens B 1965 Correction of optical distance measurements for the fluctuating atmospheric index of refraction *J. Geophys. Res.* **70** 2461–2

[19] Earnshaw K B and Owens J C 1967 A dual wavelength optical distance measuring instrument which corrects for air density *J. Quantum Electron.* **3** 544–50

[20] Meiners-Hagen K and Abou-Zeid A 2008 Refractive index determination in length measurement by two-colour interferometry *Meas. Sci. Technol.* **19** 084004

[21] Hugget G R and Slater L E 1975 Precision electromagnetic distance measuring instrument for determining secular strain and fault movement *Tectonophysics* **29** 19–27

[22] Earnshaw K B and Hernandez E N 1972 Two-laser optical distance-measuring instrument that corrects for the atmospheric index of refraction *Appl. Opt.* **11** 749–54

[23] Huggett G R 1981 Two-color terrameter *Dev. Geotectonics* **16** 29–39

[24] Meiners-Hagen K, Bosnjakovic A, Köchert P and Pollinger F 2015 Air index compensated interferometer as a prospective novel primary standard for baseline calibrations *Meas. Sci. Technol.* **26** 084002

[25] Röse A *et al* 2022 Two multi-wavelength interferometers for large-scale surveying *Proc. 5th Joint Int. Symp. on Deformation Monitoring (JISDM)* (*Valencia, Spain*) (https://doi.org/10.4995/JISDM2022.2022.13635)

[26] Minoshima K and Matsumoto H 2000 High-accuracy measurement of 240 m distance in an optical tunnel by use of a compact femtosecond laser *Appl. Opt.* **39** 5512–7

[27] Ray P, Salido-Monzú D and Wieser A 2023 High-precision intermode beating electro-optic distance measurement for mitigation of atmospheric delays *J. Appl. Geod.* **17** 93-101

[28] Minoshima K, Arai K and Inaba H 2011 High-accuracy self-correction of refractive index of air using two-color interferometry of optical frequency combs *Opt. Express* **19** 26095–105

[29] Guillory J, Truong D and Wallerand J-P 2022 Optical distance measurements at two wavelengths with air refractive index compensation *Proc. 5th Joint Int. Symp. on Deformation Monitoring (JISDM)* (*Valencia, Spain*) (https://doi.org/10.4995/JISDM2022.2022.13786)

[30] Kellerer A 2007 Assessing time scales of atmospheric turbulence at observatory sites *PhD Thesis* Astrophysics, Université Paris-Diderot—Paris VII (available at: https://theses.hal.science/tel-00171277/document)

[31] Guillory J, Teyssendier de La Serve M, Truong D, Alexandre C and Wallerand J-P 2019 Uncertainty assessment of optical distance measurements at micrometer level accuracy for long-range applications *Trans. Inst. Meas.* **68** 2260–7

[32] Guillory J, Garcia-Marquez J, Alexandre C, Truong D and Wallerand J-P 2015 Characterization and reduction of the amplitude-to-phase conversion in telemetry *Meas. Sci. Technol.* **26** 084006

[33] Braun J, Štroner M, Urban R and Dvoček F 2015 Suppression of systematic errors of electronic distance meters for measurement of short distances *Sensors* **15** 19264–301

[34] Bell B 1992 ME5000 test measurements *Proc. of the Workshop on the Use and Calibration of the Kern ME5000 Mekometer* (Stanford Linear Accelerator Center. SLAC–403)

[35] Guillory J, Truong D and Wallerand J-P 2019 Assessment of the mechanical errors of a prototype of an optical multilateration system *Rev. Sci. Inst.* **91** 2260–7

[36] ITU-R, Recommendation P.835-6 2017 Reference standard atmospheres, P series, radiowave propagation (available at: www.itu.int/rec/R-REC-P.835-6-201712-I/en)

[37] Rüeger J M 1996 *Electronic Distance Measurement: An Introduction* 4th edn (Springer)

[38] Pollinger F *et al* 2023 The European GeoMetre project—developing enhanced large-scale dimensional metrology for geodesy *Appl. Geomatics* **15** 371–81

[39] Jokela J and Häkli P 2006 Current research and development at the Nummela Standard Baseline *Proc. Shaping the Change, XXIII FIG Congress (Munich, Germany)* (available at: www.oicrf.org/-/current-research-and-development-at-the-nummela-standard-baseline)